Sticking in the quantum regime: H_2 and D_2 on Cu(100)

S. Andersson and L. Wilzén
Department of Physics, Chalmers University of Technology, S-412 96 Göteborg, Sweden

M. Persson
Institute for Theoretical Physics, Chalmers University of Technology, S-412 96 Göteborg, Sweden

J. Harris
Institut für Festkörperforschung der Kernforschungsanlage Jülich, D-5170 Jülich, West Germany
(Received 3 February 1989)

Several questions of importance have yet to be clarified concerning the sticking of a light particle on a surface. Among these are the following: the relation between permanent "sticking" and temporary "trapping," the "scaling" of the sticking coefficient with incident angle, and the role of quantum-mechanical resonance phenomena in promoting sticking. We consider these and other questions in connection with data taken for the sticking of H_2 and D_2 molecular beams in the energy range 8–45 meV and for angles of incidence between 0° and 60° on a cold (~10-K) Cu(100) surface. The sticking coefficient at zero coverage, S_0, measured with use of partial monolayer desorption, displays a background that falls off with increasing energy on which are superposed well-defined peaks at characteristic energies that coincided with features in the specular reflectivity and with the condition for "selective adsorption." The peaks are due to the formation of quasibound states that are entered via the surface corrugation, the rotational anisotropy, or both acting together, and decay via sticking and backscattering channels. These states have been studied extensively in elastic scattering measurements. We demonstrate their decay via sticking channels and show that these channels give important contributions to the resonance widths. By comparing the dependence of the observed background sticking on energy and angle with calculations, we conclude that positive-energy trapping on initial collision is prevalent at wide incident angles. The trapping probability is governed primarily by the normal rather than total energy. However, many of the trapped particles revert to the gas phase and do not contribute to the sticking coefficient. As a result, the background sticking coefficient of H_2 and D_2 on Cu(100) does not display a simple scaling behavior as the angle of incidence changes.

I. INTRODUCTION

The sticking of a gas-phase particle on a solid surface can occur in a number of ways according to the nature of the interaction with the surface. In simple cases, the important factor is the conversion and subsequent dissipation of the incident energy. For molecules that dissociate, the sticking behavior may be dominated by "steric" factors and a feature primarily of the topology of the potential energy surface or surfaces governing the dynamics. Alternatively, the molecule may stick initially as an intermediate, weakly bound "precursor"[1] in which case the dissociation probability is the product of an initial sticking, or trapping coefficient and a reaction probability for molecules that are already bound to the surface. In such cases the adsorption kinetics can be complex and depend strongly on, e.g., the surface temperature. In this paper we specifically consider particles that physisorb on the surface. There is then no significant change in the electronic configuration on adsorption, coupling to electronic excitations is expected to be very weak,[2] and the adsorption is to a very good approximation electronically adiabatic with the energy transfer occurring through the phonon system of the solid lattice. These conditions are expected to hold for rare gases adsorbing on all solids and H_2 on simple or noble metals, and may also be obtained in other cases.

In order to establish contact between theory and experiment it is crucial that the potential-energy surface governing the gas-surface collision process under study be known as well as possible. The system we consider, H_2 and D_2 molecules sticking on a Cu(100) surface, has been studied extensively over the past few years, both experimentally and theoretically. Stable physisorbed species of H_2, D_2, and HD on cold surfaces of Cu (Ref. 3) and Ag (Ref. 4) have been detected using high-resolution electron energy-loss spectroscopy. The spectra display rotational excitations and internal H—H stretch vibrations that show only minute shifts compared with the gas-phase values. This indicates that the chemical state of the physisorbed molecule is virtually identical to that of the free molecule and that rotational motion within the physisorption well is essentially unhindered. Studies of the elastic scattering of H_2 and D_2 from Cu and Ag show that the (100) and (111) surfaces are rather weakly corrugated so that the dominant interaction is one dimensional.[5–7] This interaction has been explored in detail using rotation-mediated and corrugation-mediated selective ad-

sorption and reliable level sequences and well depths are available for several surfaces, including Cu(100).[6-8] These data give a picture of the interaction that is in qualitatitive agreement with theoretical studies.[9]

A classical treatment of inelastic scattering from a lattice is justified only when typical energy transfers are large compared with the phonon bandwidth (see, e.g., Sedlmeir and Brenig[10]). In the case of H_2 on Cu, a typical value for the classical energy transfer for a molecule incident with thermal energy is $\delta\varepsilon \sim 2-3$ meV and the classical sticking coefficient therefore falls from unity to zero on an energy scale of a few meV. In preliminary reports of the present work[11] we showed that this behavior is not observed. The sticking coefficient of H_2 and D_2 on Cu(100) is of order 0.1 at low energy and falls off on an energy scale of the order of the phonon bandwidth (30 meV). This demonstrates that the sticking is in the quantum regime and cannot be described by classical mechanics. In addition, we found that the molecular rotations play an important role. Schlichting *et al.*[12] showed that the sticking coefficient of Ne on Ru(100) is also in the quantum regime and found that a quantum treatment using the so-called "forced-oscillator model" gave an adequate description of the data. Since these data were taken using effusive beams, it was not possible to measure the dependence of the sticking probability, S, on incident angle θ_i or to determine whether S displayed structure as a function of energy. As Böheim[13] and Stiles and Wilkins[14] have shown, a perturbation treatment of quantum sticking along the lines suggested many years ago by Lennard-Jones and co-workers[15] suggests that S should display a peak whenever the incidence conditions fulfill the condition for corrugation-mediated or rotation-mediated selective adsorption. This is because the incident wave is degenerate with a positive-energy trapped state and so shows resonant behavior with a buildup of amplitude in the surface region. The data published previously by three of us[11] and referred to above showed that the sticking coefficient of H_2 and D_2 on Cu(100) does display resonance structure. However, we were unable to correlate this structure with the picture of sticking that results from perturbation theory and concluded that resonant sticking occurs primarily via many-body processes involving local modes of the lattice. Further work using improved equipment and methods and sampling a wider range of incident energy and angle has established that this conclusion was too hasty. The general behavior of the sticking coefficient as a function of energy is of a smoothly varying background on which is superposed peaks at characteristic energies. However, the structure in S can indeed be associated with anomalies in the elastic scattering that correlate with the condition for selective adsorption, while the background behaves in a manner that is consistent with the standard theory of sticking via nonresonant (or "normal") phonon processes. The background is found to scale neither with the normal energy nor with the total energy but shows a dependence on incident angle intermediate between these extremes. We argue that at a large incident angle the background sticking comprises direct processes, where the total energy is lost on initial collision, and two-step processes involving a trapped positive-energy intermediate that can decay through the phonon system into negative energy states or scatter elastically or inelastically back into the gas phase.

The organization of the remainder of this paper is as follows. In Sec. II we review the sticking problem from the theoretical point of view and outline the models we have used to assist in interpreting the data. Section III is then devoted to a discussion of the experimental methods and techniques used in measuring the sticking coefficient of H_2 and D_2 on Cu(100). In Sec. IV we present data taken over a wide range of incident energies and angles and with beams having differing rotational populations. These data are then discussed extensively and compared with calculations in Sec. IV B. Finally, in Sec. V, we summarize and conclude.

II. REVIEW OF THEORY

A. The distorted-wave Born approximation and the forced-oscillator model for sticking

The "standard" theory of sticking in the quantum regime[15] is based on the distorted-wave Born approximation (DWBA) and has been described in many recent papers (see, for example, Refs. 16, 17, 14, and 18). The related, semiclassical forced-oscillator model (FOM) is a useful substitute and has the advantage that the coupling to the phonons can be treated to all orders in perturbation theory (see, for example, Refs. 10 and 19). In this section we give a brief overview of these two models and the relation between them and set up the groundwork for a discussion of the implications of the experimental results presented in Sec. IV.

The one-particle Hamiltonian, H_0, on which the perturbation theory is based comprises the adsorbed particle's center-of-mass kinetic energy T_p, the rotational kinetic energy T_Ω, and a rigid-surface potential $V_0(r,\Omega)$ that depends explicitly on the adsorbed particle center-of-mass at r, and bond orientation Ω, and implicitly on the equilibrium locations, $\{r_i\}$, of the substrate atoms. In principle, this potential depends also on the H_2 bond distance. However, in view of the large value of the vibrational quanta of H_2 and D_2 as compared with typical incident energies, this dependence can be ignored and the molecule regarded as a rigid rotor.

The eigenstates of H_0 comprise scattering states at positive energy representing elastic scattering of an incident wave from the surface, and negative-energy bound states representing particles bound to the surface. Although a one-particle problem, the determination of these states is not straightforward because the interaction couples the degrees of freedom. An incident plane wave with the molecule in a given rotational state is scattered by the surface into a series of Bragg beams involving energy transfer between directions normal and parallel to the surface, or between center-of-mass and rotational energy. Since a flat surface such as Cu(100) scatters low-energy particles primarily into the specular direction, it is usual to separate H_0 into a set of terms that describe this scattering,

$$H_\perp = T_\Omega + T_p + V_0(z) , \tag{1}$$

and a perturbation, ΔV, that describes the corrugation of the surface potential and the coupling of center-of-mass and rotational coordinates. Here, $V_0(z)$ depends only on the center-of-mass coordinate normal to the surface, z, and is defined as an average of $V_0(\mathbf{r},\Omega)$ over the remaining coordinates. The perturbation term, of course, also carries a dependence on z. Basis states defined with respect to $H_\perp$ now take the form

$$\Psi(\mathbf{r},\Omega) = u_n(z)\exp(i\mathbf{k}_\parallel\cdot\mathbf{r}_\parallel)Y_L[\Omega] , \tag{2}$$

where $Y_L[\Omega]$ is a spherical harmonic ($L\equiv\{j,m\}$), $\mathbf{k}_\parallel$ the wave vector parallel to the surface, $\mathbf{r}_\parallel$ the center-of-mass coordinate parallel to the surface, and $u_n(z)$ a solution of the one-dimensional wave equation with potential $V_0(z)$. Figure 1 illustrates the behavior of positive- and negative-energy (bound and unbound) $u_n(z)$ and shows the sequence of bound-state levels, ε_n, for H_2/Cu(100) reported previously.[8] The basis states defined by Eq. (2) are product states and are characterized by a well-defined rotational angular momentum, $\hbar\sqrt{j(j+1)}$, and parallel crystal momentum $\hbar\mathbf{k}_\parallel$.

The perturbation ΔV describes transitions between basis states (2) that are elastic in the sense that the total energy of the adsorption particle is conserved. Inelastic collisions and sticking occur as a result of an additional perturbation, $\Delta V_{\rm ph}$, that couples the particle to the phonons. For a linear coupling of the form

$$\Delta V_{\rm ph} = -\sum_i \mathbf{u}_i\cdot\mathbf{f}_i , \tag{3}$$

where $\mathbf{u}_i$ is the displacement of the ith atom and $\mathbf{f}_i$ the force exerted on this atom due to its interaction with the adsorption particle, particles described by an initial scattering state Ψ_s transfer to the bound states of $H_\perp$ at a rate given by the golden-rule expression,

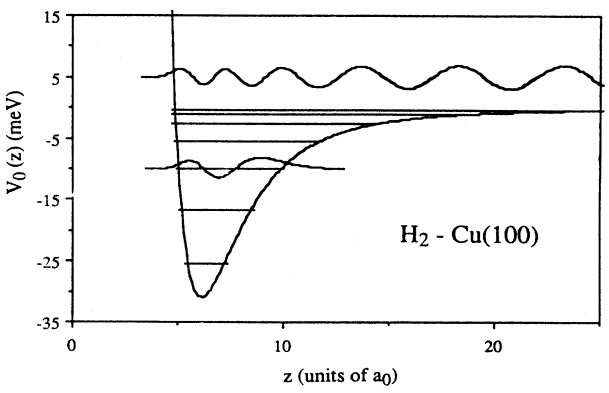

FIG. 1. Physisorption potential for H_2 on Cu(100). The position z of the molecular center of mass is given with respect to the topmost layer of ion cores. The vertical bars denote the energies of the bound-state levels. Wave functions for a scattering state with energy 5 meV and a bound-state level $n=2$ are also depicted.

$$W = \frac{2}{m_s}\sum_f \mathbf{f}^*_{sf}\cdot\frac{\mathbf{C}(\varepsilon_s-\varepsilon_f)}{\varepsilon_s-\varepsilon_f}\cdot\mathbf{f}_{sf} . \tag{4}$$

Here m_s is the mass of a substrate atom, $\mathbf{f}_{sf}$ the matrix element of the force taken between initial and final states, and

$$\mathbf{C}_{ij}(\varepsilon) = \sum_\lambda \mathbf{e}_i^\lambda \mathbf{e}_j^\lambda \delta(\varepsilon-\hbar\omega_\lambda) \tag{5}$$

is the local density-of-states tensor of the lattice. In Eq. (4) the dot product implies a sum over lattice sites and over the three directions of the forces on each site, and the sum over states "f" comprises the bound states of the particle. In Eq. (5) the sum over λ runs over the normal modes of the lattice, with $\mathbf{e}_i^\lambda$ and $\hbar\omega_\lambda$ the normalized eigenvector and energy of the normal mode labeled by λ. If the scattering state $u_{k_\perp}$ behaves asymptotically like $2\sin(k_\perp z-\delta)$, where $k_\perp$ is the incident wave vector normal to the surface and δ a phase shift, then the incident wave corresponds to a current of particles striking the surface per unit time and unit area of $\hbar k_\perp/m_p$ where m_p is the adsorption particle mass. The sticking coefficient is therefore given by

$$S = \frac{m_p W}{\hbar k_\perp} . \tag{6}$$

The semiclassical forced-oscillator model (FOM) amounts to first calculating a classical trajectory for the adsorption particle, using this to evaluate time-dependent forces $\mathbf{f}_i(t)$ acting on the lattice and determining the probability $P(\varepsilon)$ that as a result of these forces the lattice absorbs energy ε. Within the model the sticking coefficient is given as the probability that the lattice absorbs an amount of energy larger than the incident energy,

$$S = \int_{\varepsilon_i}^\infty d\varepsilon\, P(\varepsilon) . \tag{7}$$

The advantage of this model is that for a given set of forces $P(\varepsilon)$ can be evaluated without the need for a phonon expansion. Specifically, $P(\varepsilon)$ is given by

$$P(\hbar\omega) = \frac{1}{2\pi\hbar}\int_{-\infty}^{\infty} dt \exp\left[i\omega t + \hbar\int_0^\infty d\omega'\, P_s(\hbar\omega')\times(e^{-i\omega' t}-1)\right], \tag{8}$$

where

$$P_s(\epsilon) = \frac{1}{2m_s\varepsilon}\mathbf{f}^*(\varepsilon/\hbar)\cdot\mathbf{C}(\varepsilon)\cdot\mathbf{f}(\varepsilon/\hbar) \tag{9}$$

is the energy absorption function due to single-phonon processes. In Eq. (9), $\mathbf{f}(\omega)$ is the Fourier transform of the classical force and $\mathbf{C}(\varepsilon)$ the phonon density-of-states tensor given by Eq. (5). The dot product in Eq. (9) has the same meaning as in the DWBA result, Eq. (4), and the two equations show the connection between the FOM and DWBA approximations. In the former, the force matrix elements describing the transitions of the adsorption particle from a scattering state to a bound state get replaced by the Fourier transforms of the classical forces

and the sum over states by an integral over the energy loss to the phonons. As Brenig has stressed,[20] the classical treatment of the coupling in the FOM does not involve serious error. The crucial element in describing the energy transfer is the quantization of the lattice vibrations. Although Eq. (7) gives the sticking coefficient to all orders in perturbation theory, the semiclassical nature of the approximation precludes a description of resonant processes that have to do with the discrete nature of the energy spectrum of the particle (i.e., the discrete levels of the well and the rotations). The DWBA expression, Eq. (6), includes these features of the energy spectrum correctly, but is limited by the perturbation theory and so does not include resonant processes. We will refer to the sticking coefficient as given by Eqs. (6) and (7), as describing "normal," or "nonresonant," sticking and defer until later in this section the treatment of resonant contributions.

The DWBA and FOM models are both tractable and allow explicit calculations of the sticking coefficient due to normal phonon processes to be made using realistic interactions. However, when applied to non-normal incidence sticking, they both suffer from an ambiguity. Within the FOM, Eq. (7) gives the probability that at least the incident energy is lost on "the first bounce." This is clearly a lower limit for the sticking coefficient. But it also likely that some of the particles that lose less energy remain trapped at the surface and lose further energy on subsequent "bounces." For instance, one might take the view that all particles will ultimately stick that lose at least their *normal* energy on the first bounce, which would amount to replacing the lower limit of the integral in Eq. (7) by the normal rather than the total energy. A similar dilemma occurs when the DWBA is used in conjunction with the basis states in Eq. (2), which include bound states at positive energy. In writing Eq. (6) we have not specified which set of final states should be included in evaluating W. We could require that the final state have negative total energy and disregard states where the particle is in the well but has enough parallel energy to escape subsequent to the initial collision. Or we could assume that any particle that once enters the well will ultimately stick. These two criteria, like the two analogous criteria of the FOM, give very different dependences of the sticking coefficient on the angle of incidence.[19]

B. Nonresonant sticking at normal incidence

For normal incidence the transfer of parallel momentum to the particle is limited by the effective momentum cutoff in the coupling between particle and single phonons, $q_{\parallel}^{c} \approx 0.5 a_0$ (see Sec. II F). This corresponds to a parallel energy of $\hbar^2 q_{\parallel}^{c2}/2m_p \approx 1$ meV that is small compared with the important bound-state energies, typically 10 meV. Thus, virtually all final states with bound particles accessed by a normally incident beam as a result of single-phonon creation have negative total energy and the two criteria mentioned above give the same result. The DWBA sticking coefficient [Eq. (6)] for H_2/Cu(100) then depends on the incident energy as shown in Fig. 2. [The procedures used for potential and force construction and

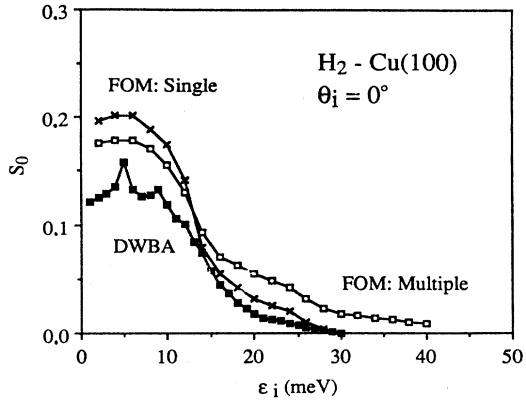

FIG. 2. Calculated sticking probabilities for H_2 on Cu(100): normal incidence. The solid squares give the results of a DWBA calculation, the crosses and open squares the results of single-phonon and multiphonon FOM calculations.

to calculate the phonon density of states tensor $\mathbf{C}(\varepsilon)$ are described in Sec. II F.] The sticking coefficient increases from zero at the bulk-phonon band edge (30 meV), but remains reasonably small until the energy sweeps through the surface-phonon band edge. The weak structure at and below 10 meV is due to processes whereby band-edge surface phonons, which give rise to sharp spikes in the phonon density-of-states [Eq. (5)] transfer particles to a specific level of the well. The overall behavior and magnitude of S is similar to that found by other workers[17,14,18] and depends only weakly on the details of the phonon spectrum.

Also shown in Fig. 2 are the results of two FOM calculations of the sticking coefficient. When the full-energy distribution in Eq. (7) is replaced by the single-phonon distribution, $P_s(\varepsilon)$, the curve marked with crosses was obtained and gives a somewhat higher level of sticking than the DWBA at lower energies. This is due in part to neglect of parallel forces in our DWBA calculation (these forces contribute about 10% to the FOM result), and in part to the smearing out of the level structure in the FOM, in particular the lack of an upper limit to the amount of energy a particle can lose. However, the correspondence is otherwise rather reasonable. The curve marked with open squares is obtained when the full-energy distribution of Eq. (8), $P(\varepsilon)$, is used in Eq. (7) and illustrates the way in which multiphonon processes alter the one-phonon picture. For low energies there is a net reduction of the sticking probability (due simply to unitarity), while towards the top of the phonon band there is a strong enhancement. This is because the large weight surface phonons contribute to the density of states, i.e., processes involving two surface phonons are as important as single bulk-phonon processes. The full multiphonon result, of course, does not vanish at the bulk phonon band edge.

Figure 2 makes clear that a one-phonon theory such as the DWBA can only be reasonably accurate at low energies where single-surface-phonon processes dominate. The correspondence between the DWBA and single-

phonon FOM results, however, suggests that the full FOM, in spite of its semiclassical nature, gives a reasonable description of multiphonon processes and so can be used in connection with data taken for higher incident energies, where the DWBA fails.

C. Nonresonant sticking at off-normal incidence: Positive-energy trapping

As remarked above the FOM and DWBA give indeterminate results for the sticking coefficient off normal incidence because of the increasing importance of positive energy trapping as the incident angle increases. Referring to the FOM, Eq. (7) still gives the probability that the particle loses all its incident energy on initial collision with the surface and so gives a lower limit for the sticking probability. An overestimate follows if the lower limit of the energy integral is replaced by *normal* energy of the particle, $\varepsilon_i \cos^2\theta_i$, to obtain the probability that at least the normal energy is lost. To the extent that the loss function $P(\varepsilon)$ is independent of the incident conditions the former prescription gives a scaling of the sticking coefficient with the total incident energy, the latter a scaling with the normal energy as the incident angle changes. In view of the acceleration of the particle by the attractive branch of the particle-surface interaction, this scaling behavior holds roughly even when the influence of the trajectory on the loss function is taken fully into account.[19] Thus, taking the FOM calculation in Fig. 2 as reference, the sticking coefficient of a 40 meV particle incident at 60° is less than 1% according to the total-energy criterion, but about 18% according to the normal energy criterion. Which of these limits, if either, is more nearly correct?

To examine this question we consider the decay of positive-energy trapped states. We assume a perfect surface in which case the only decay mechanisms available are energy loss via phonon excitation or elastic scattering back into the continuum as a result of interaction with the elastic perturbation term ΔV. Evaluating the decay rates, W_n^{inel} and W_n^{el} of positive-energy bound states ($n \equiv \{n, \mathbf{k}_\parallel\}$) scattering against the lattice, we find them to be roughly equal. These rates are sensitive to the bound-state energy but show no strong dependence on the parallel momentum $\hbar\mathbf{k}_\parallel$. A typical bound state of H_2, with $n=2$ and a parallel energy of 15 meV, corresponds to a mean free path of $l=\hbar|\mathbf{k}_\parallel|/m_p W \approx 100$ Å. Thus, on average, positive-energy trapped particles travel over large distances compared with the lattice spacing before the "sticking-reemergence" decision is made. The rough equality of the mean free paths due to scattering into sticking and reemergent channels means that neither of the two limiting cases mentioned above will obtain. Accordingly, the sticking coefficient will scale neither with the total nor with the normal energy but will lie about midway between the two.

A simple way of treating the partitioning of the particles trapped at positive energy into stuck and backscattered fractions is via a two-step model analogous to that used previously by other workers (see, for example, Refs. 20, 13, and 21). The initial collision with the surface results in a population of the bound states, P_S^0, P_T^0, where the subscripts S, T denote, respectively, states with negative and positive total energy. The results of the FOM calculation in Fig. 2 show that for normal energies below about 15 meV these populations are dominated by single-phonon events, and can be estimated reasonably via a DWBA calculation. At zero surface temperature the negative-energy particles are irreversibly stuck, while the positive-energy particles may either scatter against the phonons and lose sufficient energy to stick, or backscatter elastically or inelastically into the gas phase. Since all scattering processes within the surface well are found to give rise to broadenings and shifts of the levels in the well that are minute compared with the level spacings (e.g., an $n=2$ level of H_2 is broadened by about 0.1 meV as compared to a level spacing of about 6 meV) it is reasonable to describe the decay of the positive-energy states using a master equation formalism with transfer rates given by the golden rule. Denoting the populations of the positive-energy states at time t subsequent to the initial collision by $\mathbf{P}_T^t$, we describe their decay via

$$\frac{d\mathbf{P}_T^t}{dt} = \mathbf{W}_T \cdot \mathbf{P}_T^t \ , \tag{10}$$

where $\mathbf{W}_T$ is a rate matrix whose diagonal and off-diagonal elements represent, respectively, depletion and accumulation processes. The latter processes arise due to scattering "down the ladder" of positive-energy bound states via phonon emission and the corresponding transition rates $W_{T,nn'} = W_{nn'}^{\text{inel}}$ are given by a single term in Eq. (4):

$$W_{nn'}^{\text{inel}} = 2\pi \mathbf{f}_{nn'} \cdot \frac{\mathbf{C}(\varepsilon_{n'} - \varepsilon_n)}{2m_s(\varepsilon_{n'} - \varepsilon_n)} \cdot \mathbf{f}_{nn'}^* \ . \tag{11}$$

Depletion processes, having total rates $W_{T,nn} = -W_n^{\text{inel}} - W_n^{\text{el}}$, comprise the total inelastic scattering into bound states $(n, \mathbf{k}'_\parallel)$ and scattering states $\mathbf{p}=(\mathbf{k}'_\parallel, \mathbf{k}_\perp)$, $W_n^{\text{inel}} = \sum_{n'} W_{nn'}^{\text{inel}} + \sum_{\mathbf{p}} W_{n\mathbf{p}}^{\text{inel}}$, and elastic scattering, W_n^{el}, due either to the corrugation or to rotational transitions $L \to L'$. The elastic rate is given by a sum of transition rates to all open channels,

$$W_n^{\text{el}} = \sum_{g_\parallel, L'} \frac{2\hbar m_p}{\mathbf{k}_\perp} |\mathbf{M}_{nk_\perp}|^2 \ . \tag{12}$$

The open channels are labeled by reciprocal lattice vectors $\mathbf{g}_\parallel$ corresponding to the momentum transfer to the particle and the final rotational quantum numbers L'. The perpendicular wave vector $k_\perp$ is then fixed by energy conservation. The matrix element between initial and final states is given by

$$M_{nk_\perp} = \int dz \, u_n(z) \Delta V_{LL'}^{g_\parallel}(z) u_{k_\perp}(z) \ , \tag{13}$$

with

$$\Delta V_{LL'}^{g_\parallel}(z) = \langle\langle \, Y_{L'}^*(\Omega) \Delta V \, Y_L(\Omega) \exp(i\mathbf{g}_\parallel \cdot \mathbf{r}_\parallel) \, \rangle\rangle \ , \tag{14}$$

where the average implies integration over the orientational coordinates and center-of-mass coordinates parallel to the surface in the surface unit cell. In the case of

scattering from the surface corrugation, a nonperturbative calculation of the width showed that higher-order corrections are down typically by an order of magnitude.[22] This justifies the use of golden-rule rates in the present context.

Equations (10)–(14) define the rate problem completely and allow a numerical solution for the decay of the positive-energy bound states as a function of time. However, the fraction of the trapped particles that ends up in negative-energy states—i.e., the contribution to the sticking coefficient of the particles that trap at positive energy on the "first bounce"— can be determined directly as follows. We denote the populations of negative-energy states that build up as a result of depletion of the positive-energy fraction by $\tilde{\mathbf{P}}_S^t$. These obey the rate equation

$$\frac{d\tilde{\mathbf{P}}_S^t}{dt}=\mathbf{W}_S\cdot\mathbf{P}_T^t \tag{15}$$

with boundary condition $\tilde{\mathbf{P}}_S^0=\mathbf{0}$. Integrating, we have

$$\tilde{\mathbf{P}}_S^\infty=\mathbf{W}_S\cdot\int_0^\infty dt\,\mathbf{P}_T^t \tag{16}$$

and so, using Eq. (10), we obtain final populations of stuck states,

$$\tilde{\mathbf{P}}_S^\infty=-\mathbf{W}_S\cdot\mathbf{W}_T^{-1}\cdot\mathbf{P}_T^0\ . \tag{17}$$

A useful representation of $\tilde{\mathbf{P}}_S^\infty$ from both the conceptual and computational points of view is obtained by expanding $\mathbf{W}_T^{-1}$ in the ratio between the off-diagonal part, $\mathbf{W}^{\rm inel}$, and diagonal part, $\mathbf{W}_D$, of $\mathbf{W}_T$. That is, if we write $\mathbf{W}_T=-\mathbf{W}_D+\mathbf{W}^{\rm inel}$, then

$$\tilde{\mathbf{P}}_S^\infty=\sum_{p=0}^{\infty}\mathbf{W}_S\mathbf{W}_D^{-1}(\mathbf{W}^{\rm inel}\mathbf{W}_D^{-1})^p\mathbf{P}_T^0\ . \tag{18}$$

A term in this expansion of order p gives the contribution to the sticking probability of all $(p+2)$-phonon processes. The sticking coefficient is given by

$$S=\sum_{n_s}[\mathbf{P}_S^0+\tilde{\mathbf{P}}_S^\infty]_{n_s}\ , \tag{19}$$

where the sum is over all negative-energy states, which are labeled by n_s, comprising the discrete levels of the well and the parallel wave vector, suitably discretized. The first contribution in the square brackets arises from direct sticking on initial collision, the second via intermediate positive-energy trapping. Of course, negative-energy states will also scatter their way down the "ladder" and the final populations for all levels except the ground state will be zero. However, at zero surface temperature the transfer of particles between negative-energy states does not influence the sticking coefficient and so does not need to be treated.

Figure 3 shows three calculations of the energy dependence of the sticking coefficient for H_2/Cu(100) at 60° angle of incidence. For comparison we show also the sticking coefficient at normal incidence (open squares). The solid squares give the result of a complete calculation using Eq. (19) with proper inclusion of the partitioning of the positive-energy trapped fraction. The crosses give the

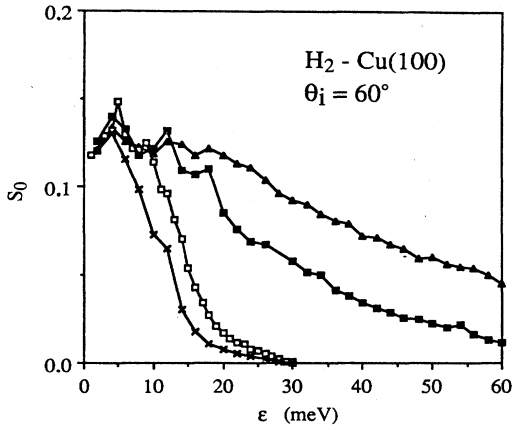

FIG. 3. Calculated trapping and sticking probabilities for H_2 on Cu(100): 60° incidence. The triangles give the trapping probability obtained via a DWBA calculation which includes all final states where the particle is bound to the surface. The crosses give the result of restricting the sum to negative-energy states. The solid squares give the sticking coefficient that results when the partitioning of the positive-energy trapped fraction into stuck and backscattered components is treated via rate equations [Eq. (19)]. The open squares give the DWBA sticking coefficient at normal incidence, included for comparison purposes.

sticking coefficient on the first bounce, obtained by including in the final state sum only those states whose total energy is negative. This corresponds to setting $\tilde{\mathbf{P}}_S^\infty=\mathbf{0}$ in Eq. (19). Note that this is a decreasing function of θ_i for fixed ε_i because the particle must "fall" sufficiently deep into the well to preclude subsequent escape via parallel and/or normal energy transfer. This effect is somewhat exaggerated in Fig. 3 because the DWBA includes only single-phonon processes (see Fig. 2) and we have neglected parallel forces. The solid triangles give the *trapping coefficient,* i.e., the result of assuming that all positive-energy trapped particles eventually stick, in which case $(\tilde{\mathbf{P}}_S^\infty=\mathbf{P}_T^0)$. The trapping coefficient falls off more slowly with energy and, as mentioned previously, is roughly the normal incidence curve on an energy scale expanded by a factor $\sim 1/\cos^2\theta_i$. As can be seen, the partitioning of the positive-energy trapped fraction leads to a result midway between the extreme limits. Accordingly, the sticking coefficient will obey no simple scaling behavior as the angle of incidence changes, i.e., will display neither approximate total energy nor approximate normal energy scaling. The weak maxima in Fig. 3 at low energy have the same origin as similar features found at normal incidence (Fig. 2), i.e., are due to processes where a specific level of the well is populated via excitation of band-edge surface phonons.

In estimating the effect of partitioning (solid squares in Fig. 3) we have neglected rotational couplings and assumed that the molecules remain always in the rotational ground state. The series expansion in Eq. (18) was evaluated using Monte Carlo sampling of the phonon momentum and the order of the phonon process. This calcula-

tion, details of which will be presented elsewhere, improves on Böheim's treatment[13] by including momentum conservation. The inclusion of momentum conservation causes the trapping coefficient fall off faster than normal energy scaling would imply.

D. Elastic scattering

A characteristic feature of particle surface scattering in the quantum regime is the nonzero probability for elastic scattering without energy transfer to the surface. The strength of the elastic scattering will of course depend on the strength of the coupling to the phonons. In the case of (H_2,D_2)/Cu(100) this coupling, $\Delta V_{\rm ph}$ is weak. In addition, the coupling to the surface corrugation or molecular rotations, ΔV, is weak. Thus the dominant event when a H_2 or D_2 molecule strikes a Cu(10) surface at low energy is an elastic, specular scattering event, and it is this feature that motivates the choice of Eq. (1) for the zeroth-order Hamiltonian. Provided the scattering is predominantly nonresonant, the strength of the specularly reflected fraction, P_0, is given reasonably by the term of lowest order in a cumulant expansion.[23] To leading order in $\Delta V_{\rm ph}$ and ΔV we have

$$P_0=\exp(-P^{\rm inel}-P^{\rm el}) , \tag{20}$$

where $P^{\rm inel}$ and $P^{\rm el}$ are, respectively, the first-order probabilities for inelastic scattering and for elastic off-specular scattering. These two probabilities are related to the corresponding inelastic and elastic rates given in Eqs. (4) and (12) in a similar manner as the sticking coefficient in Eq. (6) is related to the inelastic rate in Eq. (4). The only difference is that the sum in Eq. (4) is now over all final states and the initial bound state, n, in Eq. (12) is replaced by an incident scattering state. Note that to this order in the coupling the inelastic and elastic terms act independently. Note also that if $P^{\rm el}$ is negligible, Eq. (20) agrees with the forced oscillator result, i.e., as ε goes to zero, Eq. (8) behaves similar to Eq. (20) with $P^{\rm inel}$ given by the integral over the single-phonon loss function, $P_s(\omega)$.

E. Resonant scattering and sticking

A condition for the convergence of the cumulant expansion is that the elastic off-specular scattering is weak and can be treated in first-order perturbation theory. Since the Cu(100) surface is relatively flat, matrix elements of the elastic perturbation between the basis states of $H_\perp$ defined in Eq. (2) are rather small. Accordingly, these perturbations are negligible unless they give rise to a coupling of degenerate states of $H_\perp$. As first pointed out by Lennard-Jones and Devonshire,[15] degeneracy occurs for a scattering state with energy ε_i whenever

$$\varepsilon_i=\varepsilon_n+\varepsilon_{jj'}+\frac{\hbar^2[\mathbf{k}_\parallel+\mathbf{g}_\parallel]^2}{2m_p} . \tag{21}$$

Here, $\mathbf{k}_\parallel$ denotes the wave vector parallel to the surface of the scattering state, $g_\parallel$ a surface reciprocal lattice vector, and $\varepsilon_{jj'}$ the excitation energy for the transition between rotational states j and j'. When Eq. (21) is satisfied, a state of $H_\perp$ corresponding to pure specular scattering is degenerate with a positive-energy trapped state characterized by well-level n, enhanced parallel wave vector $(\mathbf{k}_\parallel+\mathbf{g}_\parallel)$ and/or rotational excitation energy $\varepsilon_{jj'}$, and the effect of the weak elastic perturbation ΔV is subject to resonant enhancement. In the neighborhood of a "selective adsorption" resonance, therefore, the DWBA for the sticking and inelastic scattering probabilities, as well as the cumulant expansion for the specular scattering intensity break down. To date, no fully satisfactory treatment of resonant scattering has been given. We consider now some approaches that have been taken that illustrate the nature of the problem and highlight its important features.

Selective adsorption is often discussed in terms of rigid-surface models, within which the Bragg intensities display unitarity (see, for example, Refs. 24–26). The resonances cause anomalies in the intensities of the Bragg beams which are complementary in the sense that, e.g., a dip in the specular reflectivity at resonance is accompanied by a peak in one or more of the off-specular diffraction beams. This kind of treatment is valid only when the coupling to the phonon system is weak compared with the corrugation of the stiff lattice potential. This is rarely a good approximation and is not even close to being fulfilled for the most prominent resonance structure displayed by the H_2/Cu(100) system.

An alternate approach, expressly tailored to the problem of sticking was proposed by Stiles and Wilkins,[14] who considered specifically rotationally mediated selective adsorption. These authors included the elastic perturbation giving rise to the resonance in the Hamiltonian that defines the basis states. The modified Hamiltonian then has more complex basis states, but none of them correspond to positive-energy trapped particles. The ambiguity mentioned above concerning negative-energy sticking and positive-energy trapping then does not arise and the set of states to be summed over in defining the sticking coefficient is unique. In the neighborhood of a selective adsorption resonance the incident wave builds up the amplitude near the surface and the matrix elements for all surface processes display a resonant enhancement. Stiles and Wilkins calculated the sticking coefficient for H_2 and HD interacting with Cu(100) using the DWBA and a linear coupling to describe the phonons. They found very narrow resonance lines with strong violation of unitarity. This was because of the inconsistent treatment of the perturbations. On including the elastic perturbation in the zeroth-order Hamiltonian, the decay of a selective adsorption resonance due to elastic backscattering is automatically included in the calculation to all orders in perturbation theory. However, the contribution of inelastic decays to the resonance width is not accounted for and the theory is valid only when this contribution is small compared to the elastic contributions. The strong violations of unitarity show that this condition is not fulfilled for the system H_2/Cu(100). As a corollary, it follows that *an analysis of the widths of diffraction resonances in particle-surface scattering must involve a treatment of the elastic and inelastic decays on an equal footing* and is by no means a simple matter (see, for example, Refs. 27–30).

A single-phonon formalism which fulfills this criterion was developed by Stiles, Wilkins, and Persson.[31,32] Amplitudes for zero- and one-phonon processes were obtained by solving a set of coupled-channel equations and used in DWBA-like formulas to give, e.g., the trapping probability. The theory describes the contribution of inelastic decays to the resonance width but does not include multiphonon processes such as repeated emission of phonons by positive-energy trapped particles. These kinds of processes are important when the phonon coupling and the elastic perturbation are of the same order.

A semiphenomenological theory, due to Böheim,[13] starts out from the observation that a rigid-surface treatment of narrow well-separated resonances gives probability for all events other than specular scattering of

$$P_d(\varepsilon_i)=\frac{\Gamma_i[\Gamma-\Gamma_i]}{(\varepsilon_i-\varepsilon_{\rm res})^2-\Gamma^2/4}\ , \tag{22}$$

where $\varepsilon_{\rm res}$ is the energy of the resonant state [the right-hand side of Eq. (21)] and Γ and Γ_i the total resonance width and the partial width due to decay through the incident channel. Since the probability that the resonance decays through the incident channel is given by the same expression within the square brackets replaced by Γ_i alone, Böheim interpreted the quantity

$$P_T^0(\varepsilon_i)=\frac{\Gamma_i\Gamma}{(\varepsilon_i-\varepsilon_{\rm res})^2+\Gamma^2/4}\ , \tag{23}$$

as giving the probability that the selective adsorption state was populated as a result of the collision. He averaged this population over a Maxwellian incident beam, whereupon a calculation of Γ_i alone suffices to determine initial trapping rates. These form source terms for rate equations that describe the partitioning of the trapped particles into sticking and desorbing fractions as detailed in Sec. III C. If the resonance is characterized by surface reciprocal lattice vector $g_\parallel$ and rotational transition $j\rightarrow j'$, the width Γ_i due to decay via the incident channel is given by a single term of Eq. (12),

$$\Gamma_i=\frac{2\hbar m_p}{k_\perp}|M_{nk_\perp}|^2\ , \tag{24}$$

where the matrix element between initial and final states is given by Eq. (13). The width $\Gamma^{\rm el}=\hbar W^{\rm el}$ is given by a formula analogous to Eq. (19) but involving a sum over open elastic channels. The transition rates in the rate equations are intimately related to the widths of the bound states. In the spirit of resonance theory we may write the width Γ as separate contributions

$$\Gamma=\Gamma^{\rm inel}+\Gamma^{\rm el}\ , \tag{25}$$

where $\Gamma_n^{\rm insel}=\hbar W_n^{\rm inel}$ and $\Gamma_n^{\rm el}=\hbar W_n^{\rm el}$. These expressions allow a determination of the resonance width and so the probability that the resonance decays into states corresponding to a bound particle. Böheim's scheme has the important virtues that (i) all processes are treated on an equal footing and (ii) all contributions to the resonance width can be obtained via Fermi's golden-rule-like formulas involving matrix elements that are readily calculated.

F. The interaction

We conclude this section with a brief discussion of the form of the interaction and the description of the phonons we have used in explicit calculations. A realistic modeling of the rigid-surface interaction is shown in Table I. The lateral and angular average, $V_0(z)$ [Eq. (1)], comprises a long-range van der Waals attractive branch that falls off such as z^{-3} and a repulsive branch that grows approximately exponentially as the surface is approached.[9] Recently, three of us have published a detailed study of this interaction for H_2/Cu(100) via analysis of the selective adsorption features observed in the specular reflectivity.[8] In particular, it was pointed out that the value previously accepted for the well depth was wrong by about 9 meV. The sequences of bound-state levels for H_2 and D_2 determined from the data analysis and values obtained with the potential in Table I are shown in Table II. These energies are affected only very weakly by the remaining terms in the interaction. The laterally averaged rotational coupling, denoted $V_2(z,\theta)$, is taken from theory,[9] and has strength governed by the parameters α_R (Ref. 33) and α_A (Ref. 34) for repulsive and attractive branches, respectively. The rotationally averaged lateral corrugation term in the interaction (not shown in Table I) was modeled in the manner suggested by Harris and Liebsch[35] and has amplitude function $V_{10}(z)=V_1\exp(-\beta z)$, where the exponent β is related to that of the laterally averaged potential, λ, via $\beta=\lambda/2+\{(\lambda/2)^2+[g_\parallel(10)]^2\}^{1/2}$. The strength parameter V_1 was adjusted so that calculated intensities of the lowest-order $\mathbf{g}_\parallel(10)$ Bragg beams agreed with measured values.

To determine phonon couplings we need to know how this interaction depends on the ion core locations. In performing DWBA calculations, a wave vector representation of the coupling is convenient. Since the classical turning point, z_t, of low-energy H_2 particles lies a distance from the surface plane that is considerably larger than the surface lattice spacing, the particle interacts with several neighboring surface atoms and the coupling normal to the surface is dominant. Neglecting other couplings and *umklapp* processes leads to the form for the particle-phonon coupling used previously by other authors (see, e.g., Ref. 14),

$$\Delta V_{\rm ph}(\mathbf{r},\mathbf{u}_i)=-\int_{\rm SBZ}\frac{d\mathbf{q}_\parallel}{(2\pi)^2}\frac{dV_0(z)}{dz}u_z(\mathbf{q}_\parallel)\times\exp[-(q_\parallel/q_\parallel^c)^2+i\mathbf{q}_\parallel\cdot\mathbf{r}_\parallel]\ , \tag{26}$$

where the integral runs over the surface Brilluoin zone and the momentum cutoff $q_\parallel^c=\sqrt{\lambda/z_t}$ lies well within this zone (see Table I). Using this form of the coupling we need only the derivative of the laterally and rotationally averaged potential shown in Table I together with a phonon density of states that can readily be calculated using a transfer matrix method.

In performing forced-oscillator model calculations, a site representation of the coupling is appropriate and we adopt the prescription of Eichenauer *et al.*[36] and fit the rigid surface interaction to a sum of rotationally aniso-

TABLE I. Model interaction potentials. $V_0(z)$ and $V_2(z)$ are the laterally averaged isotropic and rotationally anisotropic physisorption potentials. Their functional forms are taken from physisorption theory (Ref. 33). The parameters have been adjusted to reproduce the observed positions of the CMSA resonance structures in the elastic scattering (Ref. 8). The parameters α_R and α_A in $V_2(z,\theta)$ are taken from theory (Refs. 33 and 34). $v_0(r)$ and $v_2(r)$ are the unique isotropic and anisotropic pair potentials constructed so that a pairwise sum over surface sites reproduces $V_0(z)$ and $V_2(z,\theta)$. V_1 and β are the repulsive potential parameters for the exponential repulsive potential describing the surface corrugation (see text). V_1 has been adjusted so the potential reproduces correctly in a coupled channels calculation the measured intensity of the lowest-order Bragg beams. The exponent β is taken from physisorption theory (Ref. 41). $q_{\parallel}^c$ is the phonon momentum cutoff in the particle-phonon coupling and is determined by $V_0(z)$ (see text). The parameters given refer to an origin of z in the plane of the topmost layer of ion cores of the Cu lattice.

$$V_0(z)=V_0\exp(-\lambda z)-\frac{C_{\rm vdW}f[k_c(z-z_{\rm vdW})]}{(z-z_{\rm vdW})^3},$$

$$V_2(z,\theta)=\left[\alpha_R V_0\exp(-\lambda z)-\alpha_A\frac{C_{\rm vdW}f[k_c(z-z_{\rm vdW})]}{(z-z_{\rm vdW})^3}\right]P_2(\cos(\theta)),$$

$$v_0(r)=v\frac{\exp(-\lambda r)}{\lambda r}-\frac{C_5 h[k_c(r-z_{\rm vdW})]}{r(r-z_{\rm vdW})^4},\quad v_2(r)=\frac{v\alpha_R\exp(-\lambda r)[(\lambda r+3)\lambda r+3]}{(\lambda r)^3}-\frac{\alpha_A C_5}{r(r-z_{\rm vdW})^2}\left[\frac{h(x)}{(r-z_{\rm vdW})^2}+\frac{f(x)}{r(r-z_{\rm vdW})}+\frac{g(x)}{2r^2}\right]$$

$$x=k_c(r-z_{\rm vdW}),\quad v=\frac{A\lambda^2 V_0}{2\pi},\quad C_5=\frac{3AC_{\rm vdW}}{2\pi},$$
$$f(x)=1-(2x^2+2x+1)\exp(-2x),$$
$$h(x)=1-(4x^3/3+2x^2+2x+1)\exp(-2x),$$
$$g(x)=1-(2x+1)\exp(-2x),$$

$V_0=41.0$ eV, $\lambda=1.21a_0^{-1}$, $\alpha_R=0.18$,
$C_{\rm vdW}=4.74$ eV a_0^3, $z_{\rm vdW}=2.27a_0$, $k_c=0.45a_0^{-1}$, $\alpha_A=0.05$,
$V_1=50.6$ eV, $\beta=2.04a_0^{-1}$,
$q_{\parallel}^c=0.51a_0^{-1}$

tropic pair potentials, $v(r,\hat{\mathbf{n}}\cdot\hat{\mathbf{r}})$, centered on the surface lattice sites. The dependence on H_2 bond orientation allows for differences between the pair potentials for upright and flat molecules and is included to allow a qualitative description of the coupling between the rotational and lateral corrugations. Expanding v in Legendre functions,

$$v(r,\hat{\mathbf{n}}\cdot\hat{\mathbf{r}})=\sum_l v_l(r)P_l(\hat{\mathbf{n}}\cdot\hat{\mathbf{r}}) , \tag{27}$$

where $\hat{\mathbf{n}}$ is the molecular axis and $\hat{\mathbf{r}}$ the unit vector in the radial direction, the total potential with the molecule at $\mathbf{r}$ and with orientation $\hat{\mathbf{n}}$ is given by

$$V(\mathbf{r},\hat{\mathbf{n}})=\sum_i v(|\mathbf{r}-\mathbf{r}_i|,\hat{\mathbf{n}}[(\mathbf{r}-\mathbf{r}_i)/|\mathbf{r}-\mathbf{r}_i|]) , \tag{28}$$

where $\mathbf{r}_i$ denotes the locations of the surface atoms. Expanding in surface reciprocal lattice vectors, this can be written

$$V(\mathbf{r},\hat{\mathbf{n}})=\sum_{g_\parallel} V_{g_\parallel}(z,\hat{\mathbf{n}})\exp(i\mathbf{g}_\parallel\cdot\mathbf{r}_\parallel) . \tag{29}$$

The rotational matrix elements of $V_{g_\parallel}(z,\hat{\mathbf{n}})$ can readily be evaluated and we find rotationally isotropic and anisotropic terms

$$V_{g_\parallel}(z)\equiv\langle 0,0|V_{g_\parallel}(z,\hat{\mathbf{n}})|0,0\rangle = 2\pi\int dr_\parallel\frac{r_\parallel}{A}v_0(\mathbf{r})J_0(g_\parallel|\mathbf{r}_\parallel|) , \tag{30}$$

TABLE II. Experimental and calculated bound-state energies. The experimental bound-state energies ε_n(expt) were determined from measurements of CMSA resonances (Ref. 8). The theoretical values, ε_n(theory), were calculated numerically from the physisorption potential $V_0(z)$ given in Table I.

Molecule	Level n	ε_n(expt) (meV)	ε_n(theory) (meV)
n-H_2	0	−25.5	−25.54
	1	−16.9	−16.66
	2	−10.2	−10.07
	3	−5.8	−5.55
	4	−2.8	−2.73
n-D_2	0		−27.04
	1		−20.27
	2	−14.5	−14.68
	3	−10.3	−10.22
	4	−6.7	−6.78
	5	−4.3	−4.27
	6	−2.6	−2.53

$$V_{2,m;g_\parallel}(z) \equiv \langle 2,m | V_{g_\parallel}(z,\hat{\mathbf{n}}) | 0,0 \rangle = 2\pi c_{2m} \int dr_\parallel \frac{r_\parallel}{A} v_2(\mathbf{r}) P_2^m(z/\mathbf{r}) \mathbf{J}_m(g_\parallel |\mathbf{r}_\parallel|) , \quad (31)$$

where A is the surface area, $\mathbf{r}^2 = z^2 + \mathbf{r}_\parallel^2$, and $c_{2m} = 1/\sqrt{5}$, $1/\sqrt{30}$, $1/\sqrt{120}$ for $m = 0,1,2$. The rotationally isotropic and anisotropic pair potentials, $v_0(\mathbf{r})$ and $v_2(\mathbf{r})$, are determined uniquely by inverting Eqs. (30) and (31) and requiring that the lateral averages $V_{0,g_\parallel=0}(z)$ and $V_{2,0;g_\parallel=0}(z)$ are compatible with the potentials $V_0(z)$ and $V_2(z,\theta)$ in Table I. This inversion can be done analytically and the resulting single-site potentials are given in Table I. In estimating the strength of the nonresonant sticking using the FOM we neglect the rotational coupling so that the force $\mathbf{f}_i(\mathbf{r})$ exerted on the ith atom when the particle is at $\mathbf{r}$ can be calculated directly from the isotropic pair potential via $\mathbf{f}_i = -\nabla v_0(|\mathbf{r}-\mathbf{r}_i|)$. The phonon density of states in the site representation [Eq. (5)] can be calculated conveniently using a continued fraction method with a nearest-neighbor central force-constant model for the lattice dynamics of the semi-infinite Cu lattice.[19] The single bulk parameter in the model was adjusted to fit bulk phonon dispersion relations as measured by inelastic-neutron-scattering data,[37] and the surface interlayer force constant was stiffened by 20% over the bulk value in accordance with inelastic-electron-scattering data.[38] The model is well known to give a surprisingly good description of the bulk lattice dynamics.[39] In using a rather elaborate and state-of-the-art description of the phonons (rather than, e.g., the continuum model employed by other authors[17,14]) our main motivation has been to study the relative importance of surface and bulk phonons and the effect on the sticking of band-edge structure in the phonon density of states. A more detailed description of the lattice-dynamics calculations has been given elsewhere.[40]

The corrugation terms $\mathbf{g}_\parallel \neq \mathbf{0}$ of the isotropic and anisotropic potentials in Eqs. (30) and (31) can be calculated by numerical quadrature. As noted by other authors[36,41] in connection with He scattering from Ag and Cu phonons, the corrugation terms that result when a sum-over-sites prescription is fitted to the correct laterally averaged potential tend to be too strong. In the present case, for example, the measured intensity of the $\mathbf{g}_\parallel(10)$ Bragg beams relative to the specular intensity for D_2 at incident energy $\varepsilon_i = 45$ meV and angle $\theta_i = 70°$, is 0.081, a factor of 3 smaller than the value of 0.24 that follows if the corrugation potential Eq. (30) is used in a coupled-channels calculation. This is the reason we have used a parameterized interaction, as noted above, rather than Eq. (30) in estimating, e.g., the partial widths of resonances due to elastic scattering from the corrugation.

As Eq. (31) shows, the sum-over-sites model for the potential implies that the rotational and lateral corrugations are coupled. That is, the potential term $V_{2,m;g_\parallel}(z)$ represents a first-order coupling between an incident beam characterized by parallel wave vector $\mathbf{k}_\parallel$ and rotational state $j = 0$ with a bound state having parallel wave vector $\mathbf{k}_\parallel + \mathbf{g}_\parallel$ and rotational state $j = 2$. Thus, in addition to corrugation-mediated and rotation-mediated structure, involving the two perturbations acting independently of each other, this form of the interaction predicts structure that results from the two corrugations acting together. Such structure has been observed and will be discussed further in Sec. IV.

III. EXPERIMENT

In this section we describe experiments that measure the sticking coefficient of H_2 and D_2 molecules on a Cu(100) surface. In view of the low binding energy of physisorbed H_2 molecules, ~ 30 meV, the desorption temperature is ~ 20 K. It was therefore necessary to perform the measurements with the crystal cooled to ~ 10 K. This requirement strongly influenced the experimental procedure and the design of equipment. The apparatus used is shown schematically in Figs. 4(a) and 4(b). It consisted of a molecular-beam stage, an UHV scattering chamber, control electronics, and a data-acquisition system. H_2 (D_2) nozzle beams were shaped by skimmers in three turbopumped chambers operating at typical pressures of 1×10^{-3}, 1×10^{-6}, and 2×10^{-9} Torr, respectively. The gas was expanded from a 10-μm-diameter nozzle source at temperatures between 30 and 300 K, combining cooling by helium gas transferred from a liquid-helium Dewar and resistive heating. This technique enabled us to keep the source temperature stable to ~ 0.1 K. The hydrogen gas was precooled to liquid-nitrogen temperature before entering the nozzle source. The source temperature was controlled electronically via a thermocouple (Au 0.03% Fe–Chromel) signal and could be kept steady, ramped stepwise or linearly in time. Hydrogen pressures in the range 0.2–1.1 bars produced adequate molecular beams over the entire source temperature range with an optimum energy spread of $\sim 10\%$. The beam angular divergence was 0.29°. For the most part, measurements were made with n-H_2 and n-D_2 beams having thermal rotational populations [(even j): (odd j) = 1:3 for H_2 and 2:1 for D_2]. To determine the influence of the rotational states on the sticking a limited number of runs were performed using p-H_2 and o-D_2 beams composed solely of molecules in even-j rotational states. These beams were produced via on-line conversion of the normal gases by use of a nickel-silicate catalyst kept at 25 K by a cool helium gas flow.

The adsorption and scattering experiments were carried out in a cryopumped (1000 l/s) UHV chamber, operating at a base pressure of 3×10^{-11} Torr. The AP 6 cryopump was reconstructed so that the cooling stage could be demounted during the standard system bakeout. This construction turned out to be most satisfactory since we obtained a high pumping speed for hydrogen at low pressures and, in fact, also for helium. The chamber pressure increased to typically 5×10^{-10} Torr with the molecular beam on and pressure oscillations were negligible. Incident and scattered-beam intensities were measured using a rotatable stagnation detector with an angular resolution of 1.5°. The detector, constructed from oxygen-free high-conductance copper to minimize outgassing and charging-up effects, was equipped with a cali-

brated ionization gauge and mounted on a bellows construction enabling movement over 80° in the scattering plane and ±25° normal to the scattering plane. The pressure signal was read by an electrometer directly attached to the gauge-detector construction. This arrangement minimized microphonic noise when the detector was moved. The signal was read in a dc mode since the chamber pressure was very stable. The noise level was

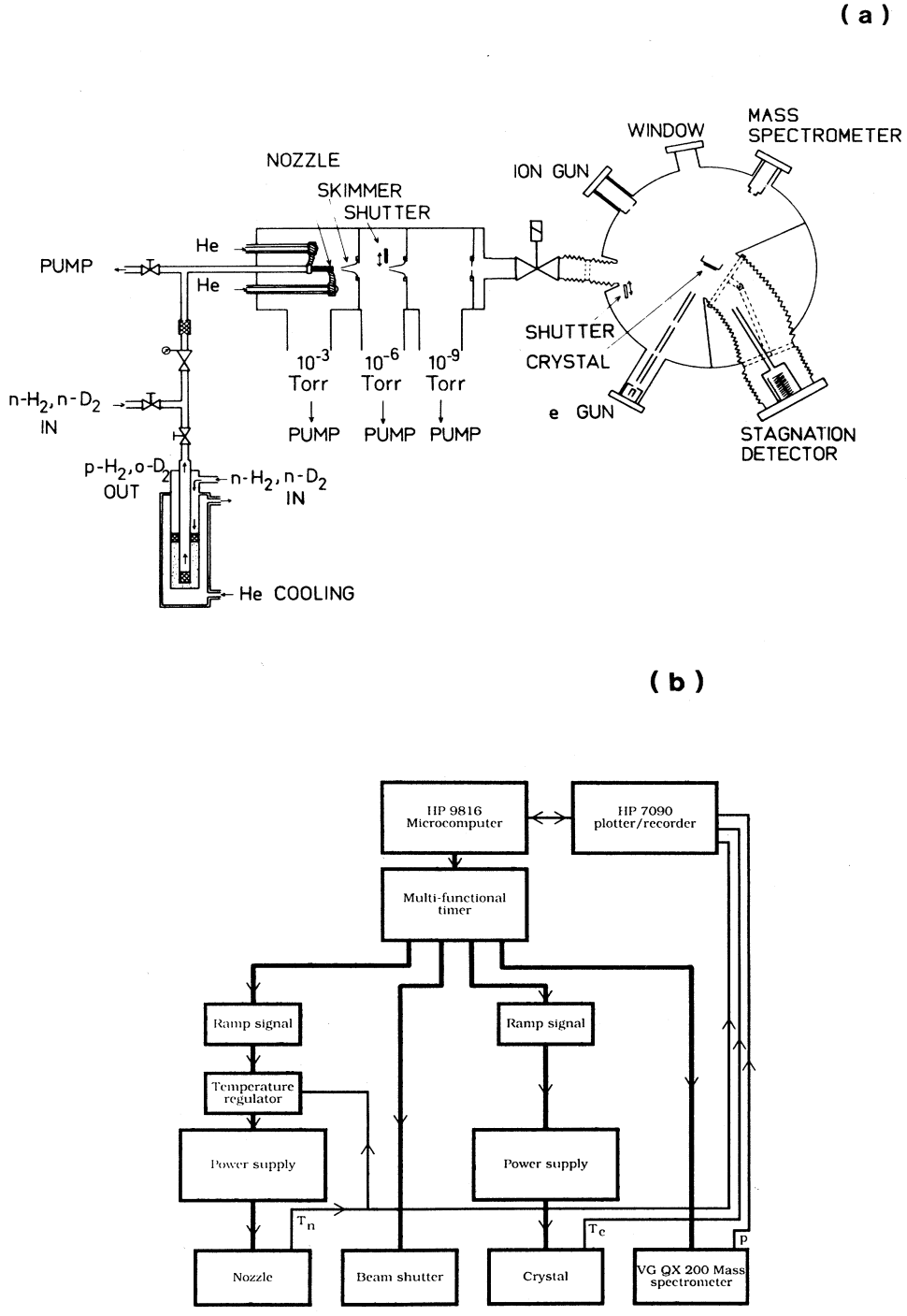

FIG. 4. Schematic drawing of (a) experimental apparatus and (b) control electronics and data-acquisition system.

less than 3×10^{-5} of the direct beam signal at an electrometer time constant of 0.3 s. Beam energies and the relative rotational populations of normal and converted gases were obtained by performing diffraction measurements using the same detection arrangement. We note that the scattering chamber, through a bellows system, could be rotated $\pm15°$ with respect to the incident molecular beam. This construction allowed straighthrough detection of the incident molecular beam and consequently increased the observable scattering angular range.

The Cu(100) specimen was spark-cut from a 99.999%-purity Cu single-crystal rod and oriented by x-ray backdiffraction to better than 0.2°. The sample was subsequently mechanically and electrolytically polished to optimal optical flatness and finish. This was achieved by alternating mechanical polishing on optical quartz flats and cloth. The electrolytical polishing in orthophosphoric acid was performed at low temperature, −40° C, in the beginning and then at −20° C. The sample was rinsed frequently in the initial stage to avoid etching caused by fine gas bubbles produced in the viscous layer. In oblique light, this layer should look under the microscope like a perfect silvery mirror. If it started to get dim the sample was immediately rinsed. The specimen was finally cleaned *in situ* by standard methods involving low-energy argon ion bombardment and heating cycles. It could be cooled to ~10 K using cool helium gas transferred from a liquid helium Dewar as cryogen and was heated resistively using an electronically controlled power supply. The Cu(100) specimen was mounted with respect to direction of the incident molecular beam so that the scattering plane comprised the surface normal and the [010] direction in the surface plane. The accuracy of this alignment was better than 0.2° as determined by diffraction measurements around the scattering plane. Out-of-plane diffraction measurements were performed in order to determine the strength of the first-order (10) diffraction beams, while the second-order (11) beams were measured in the scattering plane.

In the resonance scattering measurements discussed below the specular beam intensity, I_{00}, incident beam intensity, I_0, and nozzle source temperature, T_N, were sampled, normalized, and plotted using a Hewlett-Packard HP200-series microcomputer and a HP7090A measurement plotting system. The Cu(100) specimen was kept at about 30 K during the intensity versus T_N scans and was cleaned by flash heating to 900 K between each measurement. The scattering measurements were useful in judging the structural quality of the crystal surface. We found, using H_2 and D_2 beams, that intensity oscillations due to step interferences[42] were hardly observable even at the lowest beam energies.

The zero-coverage sticking coefficient was determined in two different ways, via the kinetics for formation of a full monolayer of physisorbed H_2 or D_2, and via partial monolayer desorption. The first method was used to establish gauge measurements at several molecular-beam energies and a few angles of incidence. For this purpose the partial H_2 (D_2) pressure was measured during the adsorption cycle by a mass spectrometer mounted on the scattering chamber. A complementary reference measurement with the chamber shutter blocking the molecular-beam path was carried out. The crystal was kept at ~10 K during both measurements and was cleaned by a heating pulse at the end of each cycle. The instantaneous adsorption rate of the Cu(100) surface was obtained from the difference of the two measurements. These data were consistent with our observation, reported previously,[43] that the sticking coefficient is strongly influenced by collisions with preadsorbed molecules and so shows a strong dependence on the coverage, Θ. Within a model that treats sticking via impact on the bare surface and via collision with a preadsorbed molecule as independent processes having probabilities S_0 and S_1, respectively, the coverage dependence of the sticking coefficient S is given by

$$S=S_0(1-\Theta)+S_1\Theta\ . \tag{32}$$

This linear behavior is demonstrated in Fig. 5, where data taken from a D_2 beam of 20-meV incident energy and 0° angle of incidence are shown. We can accordingly determine S_0 as the intercept at $\Theta=0$ of the straight line fit to the experimental data. In the actual case shown in Fig. 5 we find $S_0=0.094$. By comparison, $S_1\sim0.75$, illustrating the strong influence of collisions with preadsorbed molecules.

The second method used in measuring S_0 was partial monolayer desorption. In view of the important role of molecular collisions in promoting sticking, this method yields reliable values only when the surface coverage is small at all times during the adsorption stage. The measurement procedure was similar to that used in the first method. Since this method was used more extensively and provided the bulk of the data we give a more detailed description of the experimental procedure and instrumen-

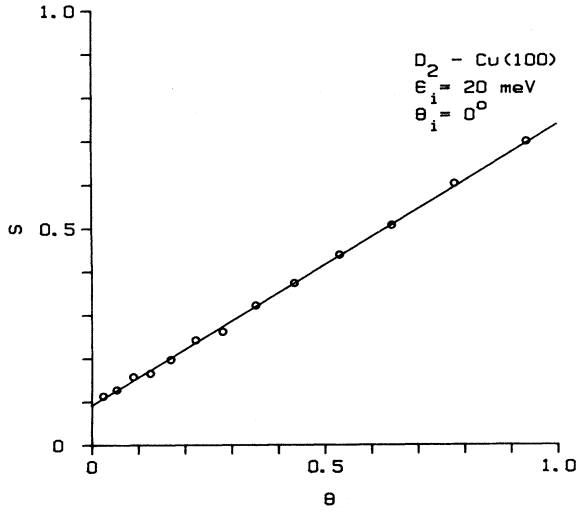

FIG. 5. Measured sticking probability, S, vs fractional adsorbate coverage, Θ, for D_2 on Cu(100) at 20 meV beam energy and 0° angle of incidence. The solid line represents a least-squares straight line fit to the data.

tation, which is shown schematically in Fig. 4(b). The measurement cycle was defined by a multifunctional timer interfaced to the microcomputer and the measurement plotting system. The timer controlled the molecular-beam pulse—via the electromechanically activated shutter in the second beam stage chamber—the specimen temperature, the nozzle source temperature, and the mass spectrometer. The computer sampled the mass spectrometer signal and the thermocouple signals from specimen and nozzle source. In a typical measurement, at fixed incident beam angle, the Cu(100) specimen was cleaned by flash heating to 900 K and allowed to cool to ~ 10 K. The H_2 (D_2) sticking coefficient was then measured at ~ 20 beam energies in a repetitive cycle which started with a specimen heating pulse that desorbed any preadsorbed H_2. A molecular-beam pulse then struck the cool (~ 10 K) Cu(100) surface and the fraction of the molecules in the pulse that stuck to the surface was determined by desorbing them via a second specimen heating pulse. Meanwhile the nozzle source temperature was ramped to set a new beam energy and a new cycle started. Each cycle took ~ 20 s. Most of the time was required to lock-in at the new nozzle source temperature. The computer instantaneously integrated the mass spectrometer signals from the beam pulse, N_I, and the desorption pulse, N_D, which were both corrected for background signals measured just before each event and subsequently calculated the sticking probability

$$S=\frac{N_D}{N_I+N_D} \tag{33}$$

as a function of incident beam energy. The sticking measurements were complemented with background measurements where the shutter in the scattering chamber blocked the molecular-beam path. Typically, H_2 adsorption from the background contributed $\sim 1\%$ to the measured sticking probability. The molecular-beam pulse time was adjusted so that any influence of collisions with preadsorbed hydrogen molecules was minimal $\leq 1\%$.

In Fig. 6 we compare sticking data obtained for D_2 beams at 0° angle of incidence using the two methods described above. The solid circles represent S_0 values derived from adsorption kinetics data while the open circles denote partial monolayer desorption data. The agreement between the two sets of measurements is fully satisfactory. Similar results were obtained at $\theta_i=40°$ and for H_2 beams at $\theta_i=0°$ and 40°. These data show that the two methods for measuring S_0 yield similar results and that the partial monolayer desorption data do refer to the zero-coverage limit, with minimal contribution due to collision with preadsorbed molecules.

We end this section with a brief discussion concerning the influence of surface imperfections on the measured sticking probability. The important role played by preadsorbed hydrogen molecules as discussed above certainly suggests that surface defects and impurities, even at concentrations of order percent, may contribute significantly. There is strong evidence that the data we present below refer to sticking on the flat surface. Firstly, the measured S_0 displays behavior that is characteristic of the flat surface and agrees satisfactorily with a theory that assumes sticking to occur solely as a result of bare-surface interactions. Secondly, by expanding the molecular beam to cover a wide portion of the crystal, the effect of, at least a certain class of defects when present in sufficient concentrations could be established. When the beam encroaches on the curved edges of the crystal, where we expect, e.g., the step density to be high, we find that S does not behave linearly at coverages close to $\Theta=0$, as in Fig. 5, but rounds off to a value that is larger than the extrapolation of the linear portion of the S-Θ curve to zero coverage. We interpret the deviation from linearity in terms of an initial "decoration" of the defects by the H_2, which, via ballistic or diffusive transport along the surface collects at the defects and passifies them. Support for this interpretation was provided by measurements made on a crystal with an overall higher defect density, which showed that a fraction of the adsorbed H_2 desorbed at a slightly higher temperature than the remainder. This suggests that the defects attract preadsorbed H_2. These findings are evidence that these defects play no major role when the molecular beam strikes only the central region of the crystal and the kinetics display a linear dependence of S on Θ. It cannot be excluded, however, that other kinds of defects that are not attractive to H_2 and so are not detected in the above manner, influence the background sticking, and in addition the widths of the resonance peaks.

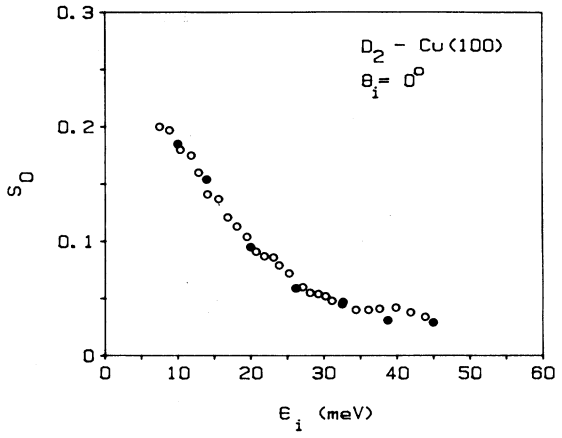

FIG. 6. Initial sticking probability, S_0, vs molecular-beam energy, ε_i, of n-D_2 on Cu(100) at 0° angle of incidence. The solid circles represent data derived from adsorption kinetics and the open circles denote partial monolayer desorption data.

IV. RESULTS AND DISCUSSION

A. Experimental results

In the preceding section we discussed the experimental procedure and showed sticking data obtained for a D_2 beam striking the Cu(100) surface at normal incidence. We now present a set of sticking data that demonstrate how the initial sticking coefficient, S_0, depends on the incident energy, ε_i, angle θ_i, and rotational population of

the impinging H_2 and D_2 beams. In general, the dependence on ε_i for fixed θ_i consists of a background contribution that falls off smoothly with increasing energy on which are superposed relatively sharp peaks centered at energies that depend strongly on θ_i. In all cases, the peaks can be assigned to a solution of the kinematical resonance, or selective adsorption condition, Eq. (21), and we have marked these solutions with arrows and the assignation as to the well-level, reciprocal lattice vector, and rotational excitation involved. In previous work we claimed to have observed resonances that could not be associated with the selective adsorption condition.[11] Peaks unequivocally connected with the molecular rotations were found at ~20 meV for D_2 at angles of incidence $\theta_i = 40°$ and 60°, and at ~45 meV for H_2 at $\theta_i = 60°$. The proximity of the energies of these structures to free-molecule rotational excitation energies ($\varepsilon_{0\to 2} = 22.2$ meV for D_2 and 44.1 meV for H_2), together with the apparent lack of dispersion, misled us into rejecting parallel momentum conserving processes as the origin. As we demonstrate below, these structures actually arise from selective adsorption processes involving a $\mathbf{g}_\parallel(10)$ reciprocal lattice vector *in combination with* the $0\to 2$ rotational transition. That is, they are due to the processes mentioned in the closing sentences of Sec. II, with the rotational and lateral corrugations of the potential acting together. The D_2 structures at 40° and 60° are not associated with the same resonance but involve different levels of the well. Far from being nondispersive, each disperses rapidly and appears in the energy window covered by the data only for a narrow range of angles. The proximity of the prominent sticking lines for the incidence conditions covered by our earlier data and the free-molecule rotational excitation energies turns out to be no more than a remarkable coincidence.

The selective adsorption resonances that give rise to peaks in the sticking coefficient are of three kinds. A *corrugation-mediated* selective-adsorption resonance (CMSA) involves a specific surface reciprocal-lattice vector, $\mathbf{g}_\parallel(hk) \neq 0$, but no rotational excitation. Such resonances are represented by $\binom{hk}{n}$ where n denotes the bound-state level involved (Table II). A *rotation-mediated* selective adsorption resonance (RMSA) involves a rotational excitation, $j \to j'$, but no diffraction

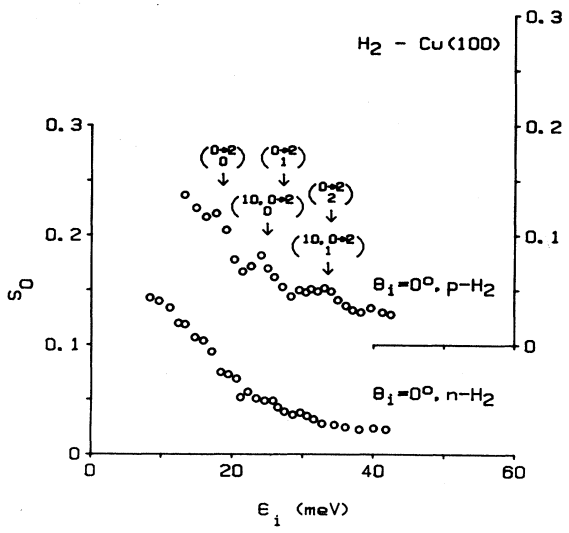

FIG. 7. Initial sticking probability, S_0, vs molecular-beam energy, ε_i, of n-H_2 and p-H_2 on Cu(100) at 0° angle of incidence.

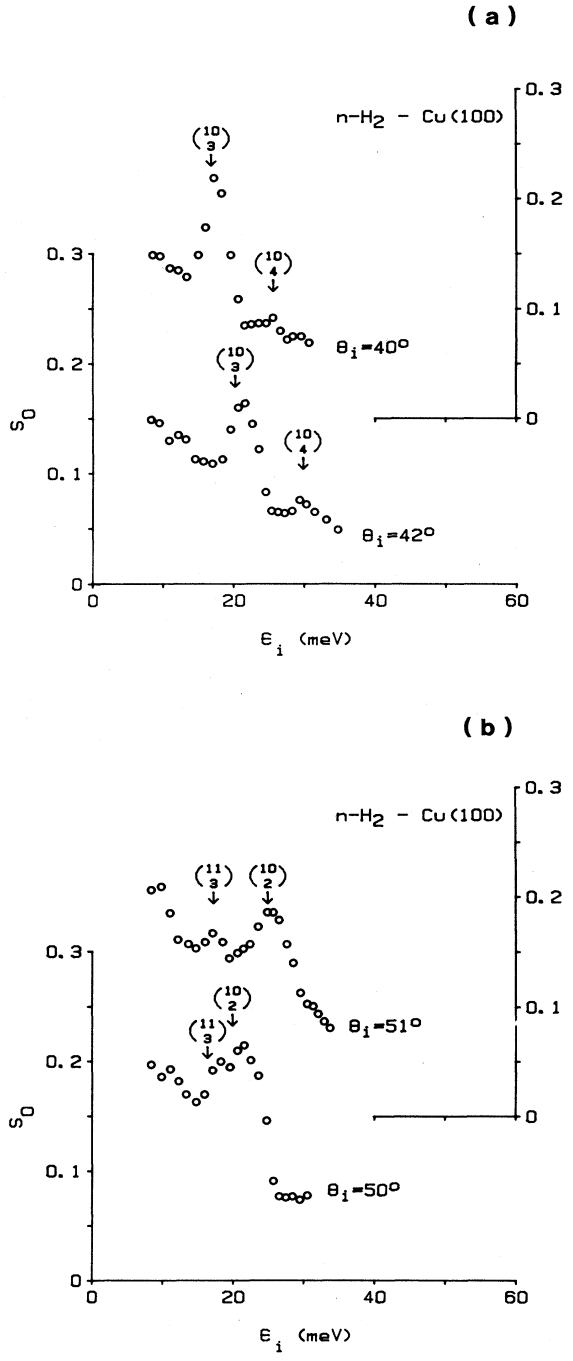

FIG. 8. Initial sticking probability, S_0, vs molecular-beam energy, ε_i, of n-H_2 on Cu(100) at (a) 40° and 42° angles of incidence and (b) 50° and 51° angles of incidence.

($\mathbf{g}_\parallel=0$) and is denoted $(^{j\to j'}_{n})$. A *combined* resonance (CRMSA) involves both rotational excitation and diffraction and is denoted $(^{hk,j\to j'}_{n})$. The nature of the resonances was established by measuring their sensitivity to the rotational population of the molecular beams and their dispersion, $\varepsilon_{\rm res}(\theta_i)$, and also by monitoring the specular reflectivity (measured with the sample at ~ 30 K). We found that *all the resonance features observed in the sticking data are also observed in the specular scattering data.* The bound-state level energies, ε_n, used in the assignation were obtained from elastic-scattering measurements, reported previously,[8] and are listed in Table II. These energies depend slightly on the rotational state of the molecule because the physisorption potential is rotationally corrugated. Scattering measurements using p-H_2 and o-D_2 beams gave ε values shifted down by ≤ 0.2 meV as compared with values obtained using the normal gases. These small differences cause only marginal shifts of the resonances discussed below and have, for simplicity, been ignored.

Figure 7 shows S_0 versus ε_i measured for n-H_2 and p-H_2 beams striking the Cu(100) surface at normal incidence, $\theta_i=0°$. The n-H_2 data show a smooth falloff of S_0 with increasing particle energy over the range 8–42 meV. For the p-H_2 beam, which was essentially of pure even j composition and hence 4 times richer in even j than n-H_2, we observe distinct resonance structure related to even j rotational transitions. The resonances are of two kinds: RMSA, $j\to j'$, $0\to 2$ ($\varepsilon_{0\to 2}=44.1$ meV); and CRMSA, $j\to j'$, $0\to 2$, and $\mathbf{g}_\parallel(10)$. The peak at 24 meV appears to be dominated by the CRMSA $(^{10,0\to 2}_{0})$.

The sticking curves in Fig. 8(a), obtained at $\theta_i=40°$ and 42°, show two CMSA resonance peaks, a rather prominent $(^{10}_{3})$ resonance and a weaker $(^{10}_{4})$ peak. These peaks coincide with anomalies in the specular reflectivity data (see I_{00}/I_0, $\theta_i=42°$ in Fig. 10). Figure 8(b) shows

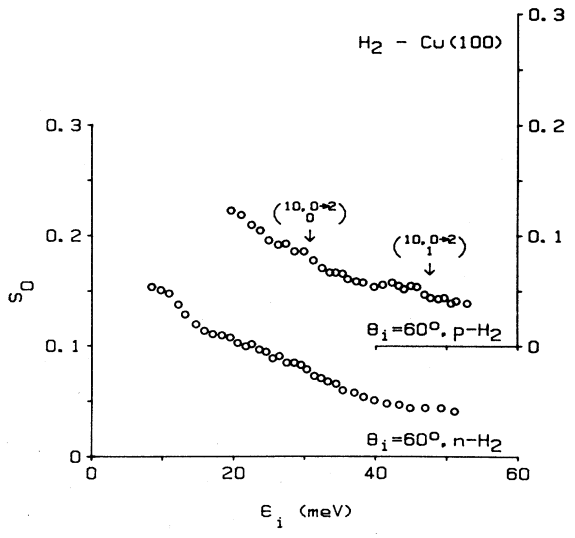

FIG. 9. Initial sticking probability, S_0, vs molecular-beam energy, ε_i, of n-H_2 and p-H_2 on Cu(100) at 60° angle of incidence.

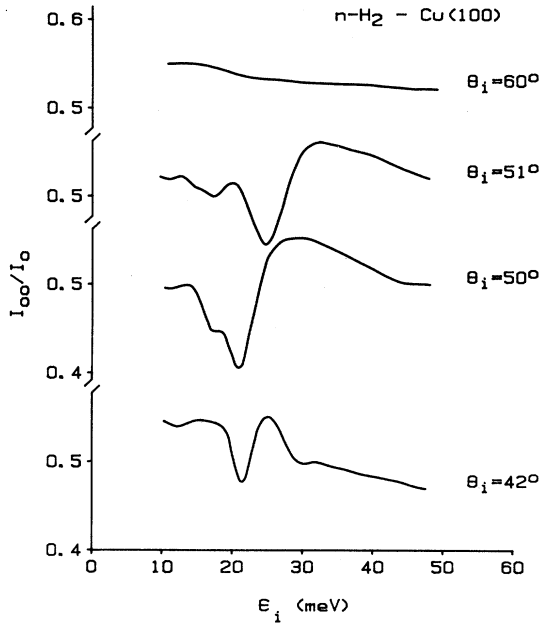

FIG. 10. Specular reflectivity, I_{00}/I_0, vs molecular-beam energy, ε_i, of n-H_2 from Cu(100) (temperature 30 K) at 42°, 50°, 51°, and 60° angles of incidence.

S_0 versus ε_i for $\theta_i=50°$ and 51°. The two peaks are assigned to CMSA resonances. The high-energy peak is clearly $(^{10}_{2})$. The low-energy peak does not coincide with a $\mathbf{g}_\parallel(10)$ resonance or a rotational transition but disperses like a $\mathbf{g}_\parallel(11)$ branch. We have tentatively assigned it as $(^{11}_{3})$. The substantial intensity is somewhat surprising, since $\mathbf{g}_\parallel(11)$ scattering is very weak. We believe this may be due to interaction with the $(^{10}_{2})$ branch. Figure 9 shows S_0 versus ε_i curves for n-H_2 and p-H_2 at $\theta_i=60°$. The p-H_2 data exhibit a weak feature around 30 meV that can be assigned to the $(^{10,0\to 2}_{0})$ CRMSA resonance, together with the feature reported earlier[8] at about 45 meV that we assign to the $(^{10,0\to 2}_{1})$ CRMSA. Specular

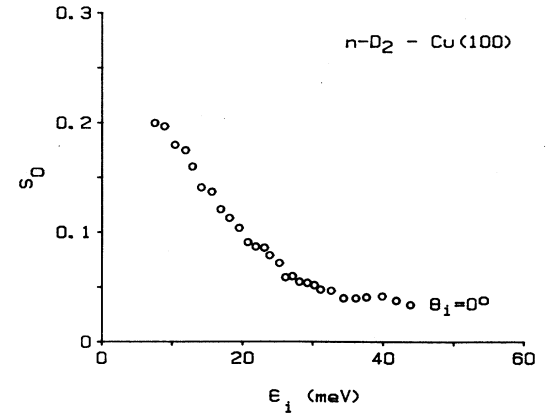

FIG. 11. Initial sticking probability, S_0, vs molecular-beam energy, ε_i, of n-D_2 on Cu(100) at 0° angle of incidence.

reflectivity curves, I_{00}/I_0 versus ε_i, obtained at $\theta_i = 42°$, 50°, 51°, and 60° are shown in Fig. 10 and illustrate the occurrence of mirror structures in reflectivity and sticking.

The sticking data for D_2 at several angles of incidence are shown in Figs. 11–13. At normal incidence (Fig. 11) we find that S_0 for n-D_2 shows a similar smooth falloff with increasing particle energy as was observed for n-H_2. Because the rotational constant of D_2 is lower than for H_2 there are closely spaced bands of RMSA and CRMSA throughout the energy range shown in Fig. 11. Thus, we were not able to resolve any rotational features for normal incidence D_2. At wide incidence, the dispersion of the CRMSA increases the level spacing and rotational structure appears in the data, as will be seen below. Figure 12(a) shows S_0 versus ε_i observed at $\theta_i = 40°$ and 42°. The data reveal a pronounced peak at low energy due to a CMSA resonance, $(^{10}_{6})$, and a weaker rotational feature assigned to the CRMSA $(^{10,0\to2}_{4})$. This is the feature reported previously.[11] The association of this feature with a rotational transition was verified via specular scattering measurements using n-D_2 and o-D_2 beams. S_0 versus ε_i plots for $\theta_i = 50°$ and 54° are shown in Fig. 12(b). The 50° data reveal two CMSA resonance peaks $(^{10}_{5})$ and $(^{10}_{6})$. The $(^{10}_{5})$ resonance is still visible in the 54° plot, which also shows a CRMSA resonance peak $(^{10,0\to2}_{3})$. Figure 13 shows S_0 versus ε_i observed at $\theta_i = 58°$ and 60°, in the latter case for both n-D_2 and o-D_2 molecular beams. The 60° data reveal two CRMSA resonances, $(^{10,0\to2}_{3})$ and $(^{10,0\to2}_{4})$, whose rotational dependence is confirmed by the o-D_2 measurements. The $(^{10,0\to2}_{3})$ resonance is also seen as a low-energy shoulder on the $(^{10}_{4})$ CMSA peak in the 58° plot. The specular reflectivity curves, I_{00}/I_0 versus ε_i for $\theta_i = 42°$, 50°, 54°, 58°, and 60°, are shown in Fig. 14 and demonstrate the strict correlation between resonance dips in the specular reflectivity and resonances peaks in the sticking data. The 60° curve shows a overall larger reflectivity and is smoother than that reported previously.[11] This is due to an improvement in surface quality.

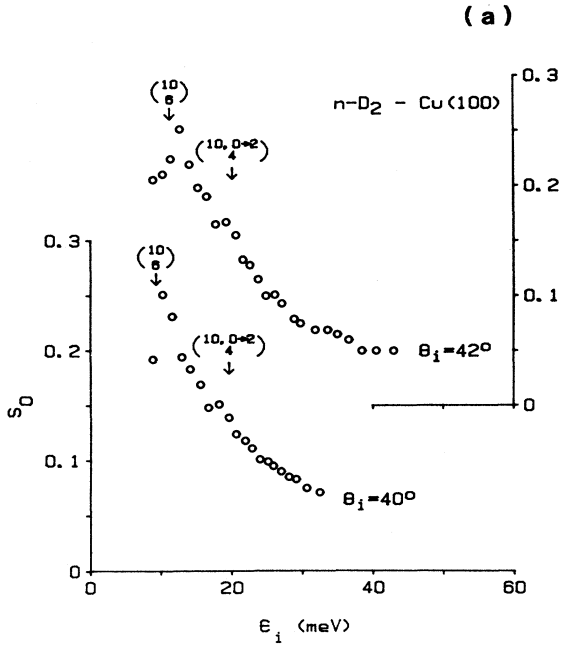

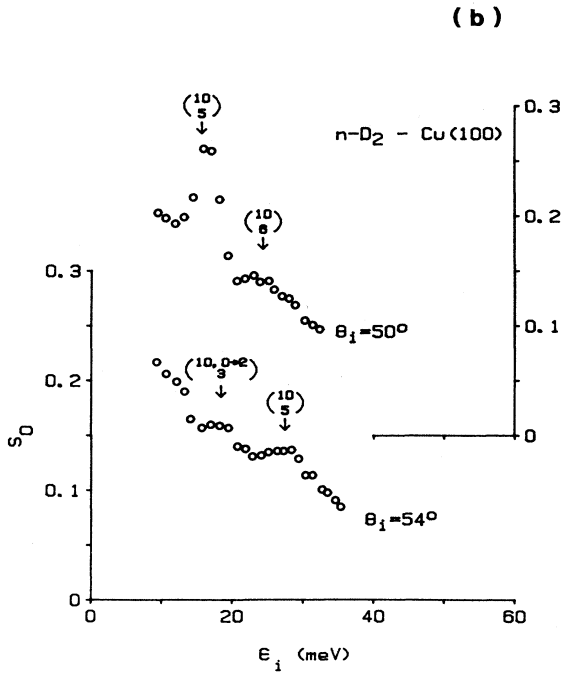

FIG. 12. Initial sticking probability, vs molecular-beam energy, ε_i, of n-D_2 on Cu(100) at (a) 40° and 42° angles of incidence and (b) 50° and 54° angles of incidence.

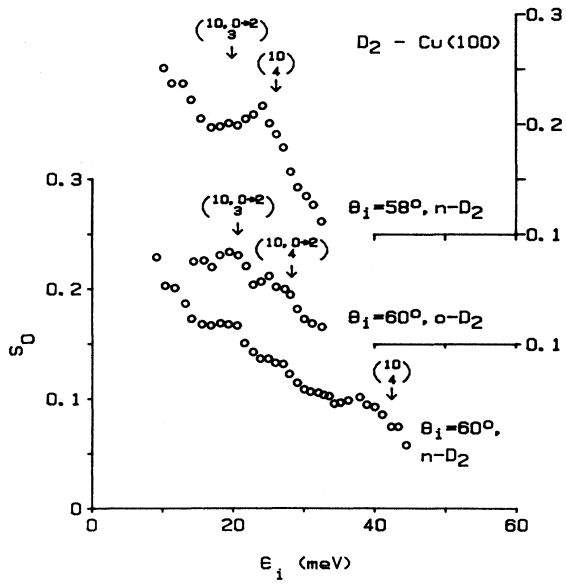

FIG. 13. Initial sticking probability, S_0 vs molecular-beam energy, ε_i, of n-D_2 and o-D_2 on Cu(100) at 58° (only n-D_2) and 60° angles of incidence.

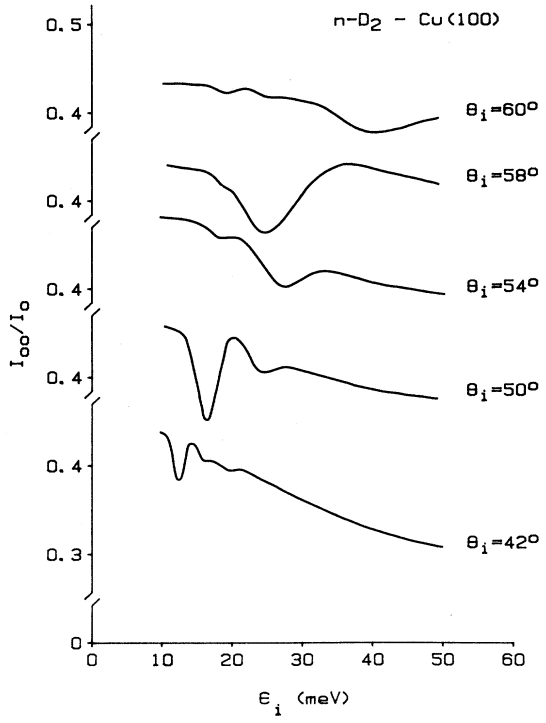

FIG. 14. Specular reflectivity, I_{00}/I_0, vs molecular-beam energy, ε_i, of n-D_2 from Cu(100) (temperature 30 K) at 42°, 50°, 54°, 58°, and 60° angles of incidence.

B. Discussion

The behavior of the zero-coverage sticking coefficient revealed by the experimental data described above is clearly in qualitative accord with standard theory based on perturbation theory and discussed in Sec. II. The observed background has the rough magnitude of the sticking expected theoretically on the basis of normal or nonresonant phonon processes, while the structure occurs for incidence conditions that agree in every case with the degeneracy, or selective adsorption criterion Eq. (21). In this subsection we attempt a more detailed comparison and focus in particular on two questions of physical interest and importance, the first being the role of positive-energy trapping, as reflected in the angle-of-incidence dependence of the background sticking. The second question concerns the strengths of the resonance lines and the reasons why some resonances show prominently in the data while others are barely resolvable.

1. Angle of incidence dependence of the background: "Scaling" behavior

From the theoretical point of view a comparison of theory with experiment is most favorable at normal incidence, where the sticking "decision" is made on initial collision (i.e., the trapping and sticking coefficients are the same). In Fig. 15 we compare the measured S_0 at normal incidence directly with DWBA and FOM calculations giving the sticking coefficient due to "normal" or nonresonant phonon processes, as described in Sec. II. As can be seen, the overall magnitude of S_0 and its energy dependence are quite reasonably reproduced. In particular, the DWBA gives a good account of the observed magnitudes at energies below about 15 meV, while the FOM gives an overestimate, as expected in view of the assumption of a bottomless well. At energies above 15 meV, where the assumption of a bottomless well is less critical, the FOM gives a good account of the observed S_0 in contrast to the dramatic falloff shown by the results from the DWBA. This observation illustrates the importance of multiphonon surface processes, which dominate the sticking at energies beyond the top of the surface-phonon bands. The theory also accounts reasonably for the isotope effect, though the comparison should not be taken too literally because the D_2 data may contain a non-negligible contribution from resonance processes, i.e., the "background" may contain a contribution from unresolved resonance lines. The resonance contribution for n-H_2 can be estimated from the strengths of the struc-

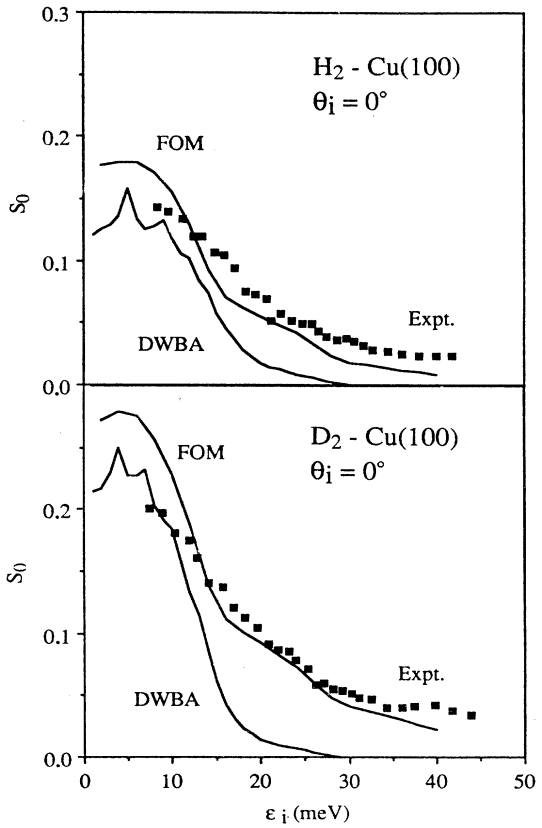

FIG. 15. Comparison of measured and calculated S_0 of H_2 and D_2 at normal incidence. The solid lines are the results of calculations using the single-phonon distorted-wave Born approximation and the multiphonon forced-oscillator model (see Fig. 2). The solid squares are the measured values (Figs. 7 and 11).

tures found for p-H_2 and is negligible. In this case the only resonances that lie within range are the RMSA and CRMSA associated with the $0\rightarrow 2$ rotational transition and the $\mathbf{g}_{\parallel}(10)$ reciprocal lattice vector.

The prevalance of resonances off normal incidence make the estimation of the nonresonant contribution difficult because the observed background may mask a significant contribution from weak, or overlapping resonances. A favorable case is H_2 incident at 60°, where the only resonances likely to give a contribution to the observed sticking are the CRMSA $(^{10,0\rightarrow 2}_{0})$ and $(^{10,0\rightarrow 2}_{1})$ which lie at about 30 and 45 meV, respectively. These resonances are visible as weak structures in the p-H_2 data and make practically no contribution for n-H_2. Accordingly, it is safe to assume that the data for H_2 at 60° reflect nonresonant sticking processes. These data are shown as solid squares in Fig. 16 together with the normal incidence data (open squares). As can be seen, the sticking coefficient is larger at the wide incidence angle for all energies for which measurements were made. This is expected because only the normal energy of the particles has to be lost on initial collision for the particle to trap at the surface. However, the data are very far from displaying a scaling with the normal energy, sometimes assumed for a flat surface. This would imply a sticking coefficient at 60° related to the sticking coefficient at normal incidence by stretching the energy scale by a factor $1/\cos^2 60° = 4$ (triangles).

To interpret the data in Fig. 16 we recall the discussion in Sec. II C and refer to the calculations summarized in Fig. 3. In this figure, the curve marked with the crosses gives within the DWBA the "first-bounce" sticking coefficient, obtained by summing over those final states

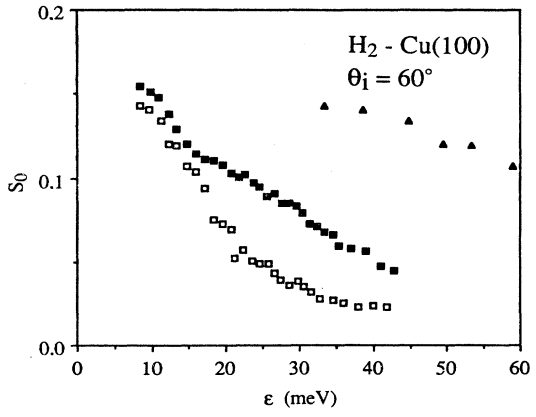

FIG. 16. Comparison of the measured sticking coefficient for H_2 at normal (open squares) and 60° (solid squares) incidence. The triangles give the sticking coefficient that would be expected at 60° incidence on the assumption of the normal energy scaling and are obtained from the normal energy data by stretching the energy scale by a factor of 4. The figure illustrates that the sticking coefficient scales neither with the normal nor with the total energy, but falls between these two limits. These data are interpreted in terms of positive-energy trapping and subsequent partitioning (see text).

where the particle has negative energy and so, at zero surface temperature, is irreversibly stuck. As can be seen, this implies a *lower* level of sticking at 60° than at normal incidence (open squares). This is because the H_2 must drop sufficiently deep in the well so that the particle cannot escape via parallel-normal energy conversion. The DWBA *trapping* probability, where the requirement is that only the normal energy need be lost on initial collision is given by the curve marked with triangles and the difference between this curve and that marked with crosses gives the positive-energy trapping probability. Finally, the partitioning of this fraction into particles which ultimately stick and those which backscatter gives the predicted sticking coefficient at 60° (squares). This actually reproduces the measured sticking coefficient reasonably well and gives a somewhat lower level of sticking, which is consistent with neglect of multiphonon processes in the initial trapping step. This we take as an indication that an interpretation of wide-angle sticking in terms of an initial trapping step and subsequent partitioning is basically correct. Note that the partitioning of the positive-energy trapped fraction as indicated in Fig. 3 depends strongly on the energy. At low energies the majority of these particles stick while at higher energies most escape. This is of course the behavior one expects since higher energy trapped particles cannot convert to the stuck fraction via a single-phonon process. A consequence of this is that the sticking coefficient at wide angles is related via simple scaling to *neither the normal nor the total energy.* That is, $S_0(\varepsilon_i,\theta_i)$ is an independent function of incident energy ε_i and angle θ_i.

Although the actual functional dependence on these variables depends on the interactions and so will differ from system to system, the basic picture underlying the theory is in no sense specific to H_2/Cu(100). We expect, therefore, that in all systems where the adsorption particle is light compared with the substrate atoms, the interaction is of the physisorption type and the sticking due primarily to phonon excitation will behave in a similar fashion. This observation may be important in connection with data taken for other adsorption systems (see, for example, Refs. 44–46 and references therein). A further consequence of the prevalence of substantial positive-energy trapping is connected with the large mean free paths of the trapped particles. Although these do not contribute to the sticking coefficient on the bare surface, they are nevertheless "on the surface" and can, for example, interact with defects and/or other adsorbed species. In the present case, for instance, the mean free path is comparable with the likely mean separation of defects so that scattering from defects may influence the partitioning and so the wide-angle sticking coefficient. This has not been accounted for in the theory because we do not possess sufficient information about the defects. We believe the effect is rather small, however. While the Cu(100) surface used in these experiments possessed no active sites where the H_2 could, for example, dissociate, the data and their interpretation do support the belief, widely held on the basis of the modeling of adsorption or reaction kinetics (see, for example, Refs. 47 and 1), that a chemical reaction can in principle be initiated by parti-

cles that arrive at the surface some distance removed from the reaction site. Furthermore, such reactions can involve particles which, if left to themselves on the bare surface, would not stick.

In concluding Sec. IV B, we compare in Fig. 17 measurements of the specular reflectivity, $P_0 = I_{00}/I_0$, with theoretical values obtained using Eq. (20). The first-order probabilities $P^{\rm el}$ and $P^{\rm inel}$ for elastic off-specular scattering and for inelastic scattering were evaluated using an exponential repulsive corrugated potential as described in Sec. II F and Eq. (26) for the particle phonon coupling. For the incidence conditions considered no rotational channels are open. The calculated values of P_0 overestimate the experimental background for both H_2 and D_2 by 10–30 %. Since the absolute value of the sticking coefficient was given rather accurately by the theory, we believe that the discrepancy evident in Fig. 17 between theory and experiment reflects primarily the absence of incoherent scattering in the theory. As is well known, surface defects have a large cross section for elastic scattering and small concentrations of them can affect the overall strength of the coherently scattered fraction quite appreciably. The calculations, of course, do not reproduce the structure in the observed reflectivities because Eq. (20) fails under resonance conditions.

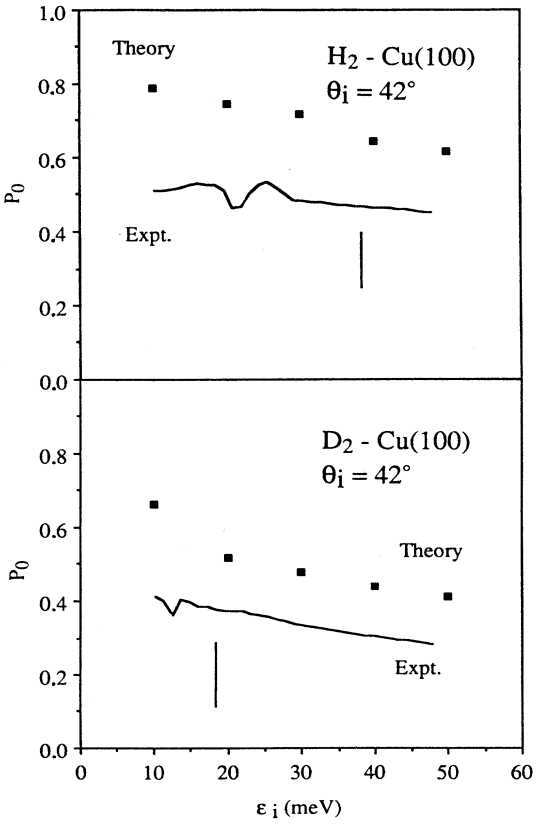

FIG. 17. Comparison of measured (solid lines) specular reflectivities for H_2 and D_2 at 42° incidence with values calculated using Eq. (20) (squares). The vertical bars indicate the thresholds for the two lowest-order Bragg beams.

2. *The resonance contribution*

In this subsection we consider the extent to which the theory in Sec. II E reproduces the observed resonance strengths, defined as the energy integrated weight of the resonance for fixed incident angle. According to Eq. (23), the probability for entering a resonant state with dispersion relation $\varepsilon = \varepsilon_{\rm res}(\mathbf{k}_\parallel + \mathbf{g}_\parallel)$, where $\varepsilon_{\rm res}(\mathbf{k}_\parallel + \mathbf{g}_\parallel)$ refers to the right-hand side of Eq. (21), is given by

$$P_T(\varepsilon_i, \Omega_i) = \frac{\Gamma_i \Gamma}{[\varepsilon_i - \varepsilon_{\rm res}(\mathbf{k}_\parallel^i + \mathbf{g}_\parallel)]^2 + \Gamma^2/4} , \tag{34}$$

where ε_i, Ω_i, and $\mathbf{k}_\parallel^i$ refer to the incident energy, angle, and parallel wave vector and Γ and Γ_i to the total width of the resonance and the partial width due to the incident channel. The resonance strength for angle Ω_i involves an integral of this probability over the incident energy. To perform this integral we note that the integrand is small unless the energy is close to ε_r, where the first term in the denominator vanishes. ε_r corresponds to the peak of the resonance line, except for a small shift of order Γ which we have ignored. Linearizing $\varepsilon_{\rm res}(\mathbf{k}_\parallel^i + \mathbf{g}_\parallel)$ around ε_r we find

$$T_{\rm tot}(\Omega) = \int d\varepsilon_i \, P_T(\varepsilon_i, \Omega_i) = \frac{2\pi \Gamma_i}{\kappa} , \tag{35}$$

where

$$\kappa = \left| 1 - \left[\frac{\partial \varepsilon_{\rm res}(\mathbf{k}_\parallel^i + \mathbf{g}_\parallel)}{\partial \varepsilon_i} \right]_{\Omega_i} \right| , \tag{36}$$

is a kinematical factor that effectively enhances the resonance width by an amount depending on the dispersion of the resonance. At wide angles of incidence, this dispersion can be very rapid and the corresponding width enhancement quite dramatic. Following Böheim the strengths of the dip in the elastic-scattering probability, $\Delta P_{\rm tot}$, and the peak in the sticking probability, $\Delta S_{\rm tot}$, are given by the product of the trapping probability into the resonance, $T_{\rm tot}$, and the relevant branching probabilities. Denoting the branching probability for sticking by $P_S^{\rm res}$ we have,

$$\begin{aligned} \Delta P_{\rm tot} &= T_{\rm tot}(\Gamma - \Gamma_i)/\Gamma , \\ \Delta S_{\rm tot} &= T_{\rm tot} P_S^{\rm res} . \end{aligned} \tag{37}$$

$P_s^{\rm res}$ is not related simply to a partial width because the resonance can decay into positive- as well as negative-energy trapped particles. Although not justified on the basis of a separation of time scales, we have treated the partitioning of positive-energy trapped decay products into sticking and backscattered fractions via rate equations, as detailed in Sec. II C.

The observed integrated strengths, $\Delta P_{\rm tot}^{\rm exp}$ and $\Delta S_{\rm tot}^{\rm exp}$, of selected sticking resonances, estimated directly from the data, are tabulated in Tables III and IV for H_2 and D_2, respectively. Also shown are the nominal degeneracies of the modes and the kinematical factors κ [Eq. (36)], evalu-

TABLE III. Measured resonance strengths: H_2. The notation for the selective adsorption resonances is described in Sec. IV A. The column labeled Degen. gives the degeneracy of the resonances under the experimental scattering conditions. $\Delta S_{\rm tot}^{\rm exp}$ and $\Delta P_{\rm tot}^{\rm exp}$ give estimates of the integrated strengths of the observed resonance peaks and dips in the sticking probability and the specular scattering probability, respectively.

	SAR	θ_i (deg)	Degen.	κ	$\Delta S_{\rm tot}^{\rm exp}$ (meV)	$\Delta P_{\rm tot}^{\rm exp}$ (meV)
n-H_2	$(^{10}_{4})$	42	2	0.34	0.1	0.2
	$(^{10}_{3})$	40	2	0.31	0.4	
		42	2	0.34	0.3	0.3
	$(^{10}_{2})$	50	2	0.11	0.7	0.7
		51	2	0.12	0.8	0.8
p-H_2	$(^{0\to 2}_{0})$	0	1	1.0	0.03	
	$(^{10,0\to 2}_{0})$	0	4	1.0	0.08	

ated using the free-particle dispersion relation Eq. (21). As can be seen, the kinematic magnification enhances the more strongly dispersing resonances by an order of magnitude and is the main reason why a rather weakly corrugated surface nevertheless gives rise to prominent sticking lines such as those evident in Figs. 8 and 12. Calculated values for the CMSA resonance strengths are shown in Table V along with the corresponding widths (unenhanced), trapping probabilities, and branching ratios. The unenhanced total widths, Γ are all of order 0.1 meV, of which between 20% and 30% is contributed by the incident channel. Column 5 of Table V shows values of the branching ratio for sticking from the resonant state, which are in the same range, 0.5–0.8, as the branching ratios into all inelastic channels (column 6). This shows that sticking is the dominant inelastic decay mode of the resonant state. Column 7 shows the branching ratio into all channels other than the incident channel. The differences between these ratios and those of column 6 give the branching into elastic channels other than the incident channel. (Where the two numbers are equal, all such channels are closed.) Finally, in columns 8 and 9, the theoretical estimates of the resonance strengths for sticking lines and specular reflectivity dips, calculated via Eq. (37), are shown. These figures are to be compared directly with the observed strengths listed in Tables III and IV. As can be seen, the calculated values are consistent overestimates, more so for D_2 than for H_2. Some possible causes are (a) slight misalignment of the crystal in the azimuthal direction which lifts the degeneracy and influences line shape and overall strength, (b) neglect in the theory of the reduction of the specular scattering intensity due to the surface collision, (c) neglect in the theory of interference effects (which can give Fano-like rather than Lorentzian line shapes), and (d) the role of defects. Given these uncertainties, we regard the agreement in order of magnitude and trend as rather reasonable.

Next, we consider RMSA resonances, for which we have calculated upper limits for the resonance strengths, given by $T_{\rm tot}$ [Eq. (35)], using the rotational corrugation in Table I. For the normal incidence H_2 $(^{0\to 2}_{0})$ RMSA we find $T_{\rm tot}=0.09$ meV, which is consistent with the observed strength of 0.03 meV if we assume a branching ratio of the same order as for the CMSA. The weakness of this resonance relative to the CMSA is due primarily to the lack of kinematic enhancement at normal incidence and the absence of degeneracy for RMSA. However, there are enhanced RMSA at wide-angle incidence and, for example, our calculation for the $(^{0\to 2}_{2})$ RMSA of D_2 at 60° angle of incidence, which lies at an incident energy of 31 meV, gives $T_{\rm tot}\sim 2.2$ meV. If the branching ratio were of order 0.3, this resonance would be clearly visible in the o-D_2 data, which it is not (Fig. 13 for the sticking and Fig. 14 for the specular reflectivity). In fact, the normal incidence H_2 $(^{0\to 2}_{0})$ RMSA referred to above is the

TABLE IV. Measured resonance strengths: D_2. Same as for Table III.

	SAR	θ_i (deg)	Degen.	κ	$\Delta S_{\rm tot}^{\rm exp}$ (meV)	$\Delta P_{\rm tot}^{\rm exp}$ (meV)
n-D_2	$(^{10}_{6})$	42	2	0.30	0.1	0.09
		50	2	0.22	0.06	0.1
	$(^{10}_{5})$	50	2	0.17	0.3	0.4
		54	2	0.15	0.2	0.3
	$(^{10}_{4})$	58	2	0.066	0.9	0.7
		60	2	0.081		0.5
o-D_2	$(^{10,0\to 2}_{3})$	60	2	0.49	0.08	0.06
	$(^{10,0\to 2}_{4})$	60	2	0.45	0.1	0.06

only RMSA to have been identified unequivocally in the data. One possible explanation for the nonobservation of wide-angle RMSA that corresponds to substantial values of T_{tot} is that the branching ratio for inelastic versus elastic scattering becomes increasingly unfavorable as the parallel kinetic energy increases. This is consistent with the fact that the CRMSA resonances that give prominent sticking lines involve diffraction processes where the parallel momentum in the final state is reduced over the incident value (i.e., the resonance condition involves $\mathbf{k}_\parallel - \mathbf{g}_\parallel$ rather than $\mathbf{k}_\parallel + \mathbf{g}_\parallel$).

Whereas only one single RMSA has unequivocally been identified in the sticking and reflectivity data, several CRMSA have been observed both for H_2 and D_2. Theoretical analysis of the CRMSA is complicated because there are contributions to the widths that first appear only in second-order perturbation theory that nevertheless, when treated to all orders, are of a similar magnitude as the first-order terms referred to in Sec. II and devolving solely from the combined rotational and lateral corrugations. Accordingly we have made separate estimates of the contributions to T_{tot} arising from these two perturbations. The first uses the joint corrugation perturbation [Eq. (31) with $\mathbf{g}_\parallel(10)$] and the golden rule. The second uses a coupled-channels method to treat to all orders the effect of the combined perturbations $V_{10}(z)$, and $V_{2,m:\mathbf{g}_\parallel=0}(z)$ in Eq. (31). In first order, these perturbations give rise only to CMSA and RMSA, respectively. We refer to the two types of processes, as rot/corr and rot+corr, and find that they contribute roughly equal widths. For the $(^{10,0\to 2}_{3})$ and $(^{10,0\to 2}_{4})$ CRMSA of D_2 at 60° angle of incidence, for example, the rot/corr processes contribute 0.10 and 0.27 meV to T_{tot}, while rot+corr terms contribute 0.07 and 0.20 meV, respectively. These figures include all summations over the azimuthal rotational quantum numbers, enhancement factors and degeneracies and can be compared directly with the measured strengths of 0.06 and 0.07 meV quoted in Table IV. These figures are consistent with the calculated values of T_{tot} provided the branching ratio is of the same order as for the CMSA processes.

This situation does not obtain for other CRMSA's, however. The $(^{10,0\to 2}_{0})$ CRMSA of H_2 at normal incidence is estimated to have total strengths T_{tot} due to rot/corr processes and rot+corr processes of about 0.006 and 0.008 meV, respectively. These figures are small because there is no kinematic enhancement at normal incidence and matrix elements linking scattering states with the ground state of the well are rather small. The measured strength, however, is estimated to be 0.08 meV (Fig. 7), a factor of 6 *larger* than the theoretical upper limit. This discrepancy cannot be due to unfavorable branching ratios but could, possibly, be due to resonance interference. The CRMSA in question lies close to the $(^{0\to 2}_{1})$ RMSA resonance, which has an estimated *total* strength of 0.16 meV and so should be more prominent than both the neighboring CRMSA *and* the corresponding $(^{0\to 2}_{0})$ RMSA, which is clearly resolved in the data. Conceivably, the higher-lying RMSA resonance may be masked by the lower-lying CRMSA, which becomes enhanced. The same effect could account for the nonobservance of the D_2 60° $(^{0\to 2}_{2})$ RMSA resonance mentioned

TABLE V. Calculated resonance strengths: H_2 and D_2. Γ and Γ_i give the total resonance width and partial width due to the entrance channel, respectively. T_{tot} is the integrated strength for entering the resonance and includes both the kinematical factor [Eq. (35)] and the nominal degeneracy. P_s^{res} gives the probability that the decay of the resonance results in sticking of the particle. This includes both direct decay processes and indirect processes where the resonance decays into a positive-energy state which subsequently converts to a negative-energy state via phonon creation. $(\Gamma-\Gamma_i)/\Gamma$ gives the probability for decay of the resonance via all other channels than the incident channel. ΔS_{tot} and ΔP_{tot} are the final theoretical estimates of the integrated strengths of the resonance peaks and dips in the sticking probability and the specular scattering probability, respectively, and are to be compared directly with the observed strengths in Tables III and IV.

	CMSA	θ_i (deg)	Γ (μeV)	T_{tot} (meV)	P_s^{res}	$\frac{\Gamma_{inel}}{\Gamma}$	$\frac{\Gamma-\Gamma_i}{\Gamma}$	ΔS_{tot} (meV)	ΔP_{tot} (meV)
n-H_2	$(^{10}_{4})$	40	56	0.38	0.46	0.55	0.80	0.15	0.30
		42	55	0.41	0.49	0.56	0.80	0.15	0.33
	$(^{10}_{3})$	40	71	0.73	0.66	0.75	0.75	0.49	0.55
		42	64	0.74	0.69	0.73	0.73	0.42	0.54
	$(^{10}_{2})$	50	75	2.4	0.77	0.72	0.72	1.5	1.7
		51	75	2.1	0.73	0.73	0.73	1.3	1.5
n-D_2	$(^{10}_{6})$	40	57	0.61	0.70	0.72	0.72	0.43	0.44
		42	58	0.67	0.72	0.72	0.72	0.48	0.48
		50	68	0.80	0.46	0.56	0.79	0.37	0.63
	$(^{10}_{5})$	50	101	1.5	0.55	0.55	0.80	0.81	1.2
		54	100	1.5	0.50	0.59	0.82	0.76	1.2
	$(^{10}_{4})$	58	119	4.2	0.53	0.56	0.82	2.2	3.4
		60	120	2.8	0.52	0.63	0.85	1.5	2.4

above. This should lie at 31 meV and could be masked by the $(^{10,0\rightarrow 2}_{4})$ CRMSA, which lies at 28 meV. In this case, however, the strength of the CRMSA was compatible with the calculated T_{tot} and not anomalously large. No simple interpretation, therefore, can explain plausibly the erratic relation between calculated and measured RMSA and CRMSA resonance weights and we suspect that the theory is missing some essential element, possibly connected with the rotation-phonon coupling.

A significant observation appears to be the anomalous strength of the CRMSA *vis à vis* the corresponding RMSA. This seems to suggest that substantial rotational inelasticity requires participation of $\mathbf{k}_{\parallel}\neq 0$ lattice modes, which is in accord with experience in inelastic H_2 scattering. Allison and Feuerbacher found[48] that rotational structure in the time-of-flight spectra when H_2 and D_2 were scattered from a LiF(100) surface dispersed with scattering angles. They interpreted this observation in terms of joint events involving both rotational excitation and excitation of surface phonons. A similar observation was made by Brusdeylins and Toennies,[49] who scattered D_2 from NaF. More recently, it has been found that single-phonon lines can carry stronger rotational satellites than the zero-loss line.[50] A feature of the rotation-phonon coupling that may have an important bearing on these observations concerns the conservation of angular momentum. In a collision between a molecule and a single atom, a molecular rotation can be excited only in conjunction with a counter rotation of the combined system. When the atom is embedded in a surface, the force responsible for the counterrotation acts in the parallel direction and can excite phonons. Further theoretical work on the rotation-phonon coupling incorporating this effect is underway and will be reported elsewhere.

V. SUMMARY AND CONCLUSIONS

The data presented above for H_2/Cu(100) or D_2/Cu(100) demonstrate behavior that we believe is typical for the sticking of light, inert particles on surfaces in the zero-coverage limit. The sticking processes are inherently quantum in nature and a theory based on perturbative coupling to phonons accounts satisfactorily for most of the data. This is evidence that phonon excitation is the dominant energy-transfer mechanism in such systems. Sticking occurs via *normal* and *resonant* processes. Normal, or nonresonant processes involve the trapping of the particle on initial impact via inelastic scattering from the phonon system and contribute a background sticking that falls off smoothly with incident energy on an energy scale set by the width of the phonon bands. Surface phonons make a proportionally greater contribution to the sticking than bulk phonons because their eigenvectors are more strongly weighted on surface sites. As a result, multiple–surface-phonon processes dominate the sticking even within the bulk phonon band. The background sticking for a given incident energy tends to increase with incident angle but does not scale with the normal energy or with the total energy. The observed behavior has been adequately reproduced via a two-step theory comprising a trapping step and partitioning of the fraction of particles trapped at positive energy into sticking and reemergent channels. The theory shows that positive-energy trapping is prevalent at wide incident angles and that the mean free paths of the trapped particles are long compared with the lattice spacing. A fraction of the particles trapped at positive energy is scattered back into the gas phase and so does not contribute to the sticking coefficient. The relative weight of this fraction as compared with the fraction that sticks on the surface increases with energy. Particles trapped with considerable parallel kinetic energy may collide with defects or adsorbed species and contribute to the rates of surface reactions, even though on the clean, defect-free surface they do not necessarily contribute to the sticking.

Resonant processes contribute a peak structure to the sticking and occur via the formation on initial collision of a *quasibound* state. Contrary to the interpretation given to preliminary data in an earlier report,[11] all resonances that contribute to the sticking can be associated with a solution of the condition for *selective adsorption.* Accordingly, the correct picture of resonant sticking is that given previously by Böheim,[13] and involves an initial *elastic* collision into the resonant state. The resonant bound state is accessed from the initial scattering state via matrix elements arising from the lateral corrugation of the surface potential, the rotational asymmetry of the interaction, or both acting together. The resonant state decays via the incident channel, other open elastic channels, or inelastic channels including trapping or sticking channels. The observation of peaks in the sticking coefficient confirms that inelastic channels make an important contribution to the resonance widths, as shown by explicit calculations of the partial widths. As a result, the behavior of the elastic channels (Bragg beams) at and near resonance cannot, in general, be reproduced within an elastic-scattering-only theoretical model. In all cases where resonance peaks were observed in the sticking coefficient, mirror structures were found in the specular scattering intensity. Values for the strengths of the corrugation-mediated resonances in the sticking coefficient and the specular reflectivity, calculated using a model interaction that reproduces the observed bound-state energies and the intensities of the dominant Bragg beams, agreed with measured strengths in trend and order of magnitude. The same was not true of rotation-mediated and rotation-plus-corrugation–mediated resonances. Structure due to rotation-mediated resonances tended to be weaker than expected, while the combined resonances were stronger than expected.

ACKNOWLEDGMENTS

We thank W. Brenig, D. Langreth, B. Lundqvist, R. Ryberg, M. Stiles, and Ch. Wöll for useful discussions and comments and R. Johansson for his excellent technical work. Financial support from the Swedish Natural Science Research Council (NFR) is gratefully acknowledged.

[1]D. A. King and M. G. Wells, Proc. R. Soc. London, Ser. A **339**, 245 (1974); D. J. Auerbach and C. T. Rettner, in *Kinetics of Interface Reactions,* edited by M. Grunze and H. J. Kreuzer (Springer, Berlin, 1987), p. 125; M. D. Williams, D. S. Bethune, and A. C. Luntz, J. Chem. Phys. **88**, 2843 (1988).
[2]K. Schönhammer and O. Gunnarsson, Phys. Rev. B **22**, 1629 (1980).
[3]S. Andersson and J. Harris, Phys. Rev. Lett. **48**, 545 (1982).
[4]Ph. Avouris, D. Schmeisser, and J. E. Demuth, Phys. Rev. Lett. **48**, 199 (1982).
[5]J. Perreau and J. Lapujoulade, Surf. Sci. **121**, 341 (1982).
[6]C.-F. Yu, K. B. Whaley, C. S. Hogg, and S. J. Sibener, Phys. Rev. Lett. **51**, 2210 (1983); J. Chem. Phys. **83**, 4217 (1985).
[7]M. Chiesa, L. Mattera, R. Musenich, and C. Salvo, Surf. Sci. **151**, L145 (1985).
[8]S. Andersson, L. Wilzén, and M. Persson, Phys. Rev. B **38**, 2967 (1988).
[9]P. Nordlander, C. Holmberg, and J. Harris, Surf. Sci. **152**, 702 (1985).
[10]R. Sedlmeir and W. Brenig, Z. Phys. B **36**, 245 (1980).
[11]S. Andersson, L. Wilzén, and J. Harris, Phys. Rev. Lett. **55**, 2591 (1985); **57**, 1603 (1986).
[12]H. Schlicting, D. Menzel, T. Brunner, W. Brenig, and J. C. Tully, Phys. Rev. Lett. **60**, 2515 (1988).
[13]J. Böheim, Surf. Sci. **148**, 463 (1984).
[14]M. D. Stiles and J. W. Wilkins, Phys. Rev. Lett. **54**, 595 (1985).
[15]J. E. Lennard-Jones and C. Strachan, Proc. R. Soc. London, Ser. A **150**, 442 (1937); J. E. Lennard-Jones and A. F. Devonshire, *ibid.* **158**, 253 (1935).
[16]F. O. Goodman, Surf. Sci. **92**, 185 (1980); **111**, 279 (1981).
[17]J. Stutzki and W. Brenig, Z. Phys. B **45**, 49 (1981).
[18]G. Armand and J. R. Manson (unpublished).
[19]M. Persson and J. Harris, Surf. Sci. **187**, 67 (1987).
[20]W. Brenig, Phys. Scr. **35**, 329 (1987).
[21]Z. W. Gortel, H. J. Kreuzer, and R. Teshima, Phys. Rev. B **22**, 5655 (1980).
[22]M. Persson (unpublished).
[23]V. Celli and A. A. Maradudin, Phys. Rev. B **31**, 825 (1985).
[24]K. L. Wolfe and J. H. Weare, Phys. Rev. Lett. **41**, 1663 (1978).
[25]K. B. Whaley, J. C. Light, J. P. Cowin, and S. J. Sibener, Chem. Phys. Lett. **89**, 89 (1982); K. B. Whaley, C. Yu, C. S. Hogg, J. C. Light, and S. Sibener, J. Chem. Phys. **83**, 4235 (1985).
[26]R. Schinke, Surf. Sci. **127**, 283 (1983).
[27]L. Greiner, H. Hoinkes, H. Kaarman, H. Wilsch, and N. Garcia, Surf. Sci. **94**, L195 (1980).
[28]J. S. Hutchison, Phys. Rev. B **22**, 5671 (1980).
[29]P. Cantini, S. Terreni, and C. Salvo, Surf. Sci. **109**, L491 (1981).
[30]V. Celli, A. M. Marvin, and G. Benedek, Surf. Sci. **148**, 54 (1985).
[31]M. D. Stiles, J. W. Wilkins, and M. Persson, Phys. Rev. B **34**, 4490 (1986).
[32]M. D. Stiles and J. W. Wilkins, Phys. Rev. B **37**, 7306 (1988).
[33]P. Nordlander, C. Holmberg, and J. Harris, Surf. Sci. **175**, L753 (1986).
[34]J. Harris and P. J. Feibelman, Surf. Sci. **115**, 133 (1982).
[35]J. Harris and A. Liebsch, Phys. Rev. Lett. **49**, 341 (1982).
[36]D. Eichenauer, U. Harten, J. P. Toennies, and V. Celli, J. Chem. Phys. **86**, 3693 (1986).
[37]E. C. Svensson, B. N. Brockhouse, and J. M. Rowe, Phys. Rev. **155**, 619 (1967).
[38]M. Wuttig, R. Franchy, and H. Ibach, Solid State Commun. **57**, 445 (1986).
[39]J. E. Black, F. C. Shanes, and R. F. Wallis, Surf. Sci. **133**, 199 (1983).
[40]M. Persson, Phys. Rev. B **36**, 7870 (1987).
[41]A. Liebsch and J. Harris, Surf. Sci. **123**, 355 (1982).
[42]J. Lapujoulade, Surf. Sci. **108**, 526 (1981).
[43]L. Wilzén, S. Andersson, and J. Harris, Surf. Sci. **205**, 387 (1988).
[44]D. J. Auerbach, H. E. Pfnür, C. T. Rettner, J. E. Schlaegel, J. Lee, and R. J. Madix, J. Chem. Phys. **81**, 2515 (1985).
[45]C. T. Rettner, H. E. Pfnür, and D. J. Auerbach, Phys. Rev. Lett. **54**, 2716 (1985).
[46]A. C. Luntz, M. D. Williams, and D. S. Bethune, J. Chem. Phys. **89**, 4381 (1988).
[47]P. Kisliuk, J. Phys. Chem. Solids **3**, 95 (1957); **5**, 78 (1958).
[48]W. Allison and B. Feuerbacher, Phys. Rev. Lett. **45**, 2040 (1980).
[49]G. Brusdeylins and J. P. Toennies, Surf. Sci. **126**, 647 (1983).
[50]G. Brusdeylins (private communication).